The Central Amygdala Encodes Nutritional Properties and Modulates Weight Gain

A Dissertation by

Sara Elizabeth Boyle

To

The School of Biological Sciences at
Cold Spring Harbor Laboratory

In Partial Fulfillment
of the Requirements for the Degree of
Doctor of Philosophy in Biological Sciences

Bo Li Lab
April 2023

Table of Contents

List of Tables and Figures

List of Abbreviations:

AGRP: Agouti-related protein, neuronal cell type marker
AP: area postrema
ARC: hypothalamic arcuate nucleus
Amb: ambiguous nucleus
BA: basal amygdala
BAT: brown adipose tissue
BF: basal forebrain
BLA: basolateral amygdala
CC: central canal
CCK: cholecystokinin, anorexigenic hormone linked to digestion
CRH: Corticotropin releasing hormone gene, neuronal cell type marker
CS: conditioned stimulus
CTXin: insula cortex
CTXs: sensory cortex
CeA: central amygdala
CeL: lateral division of the central amygdala
CeM: medial division of the central amygdala
ChR2: channelrhodopsin, light-gated ion channel that allows influx of cations, causing depolarization (activation) of neurons
DMH: Dorsomedial hypothalamus
DMV: dorsal motor nucleus of the vagus
Drd2: dopamine D2 receptor gene, neuronal cell type marker
GLP-1: glucagon-like peptide 1
HYP: hypothalamus
Htr2a: serotonin 5-HT2A receptor gene, neuronal cell type marker
IRt: reticular formation
ITC: intercalated neurons
LA: lateral amygdala
LC: locus coeruleus
LH: lateral hypothalamus
LPS: bacterial lipopolysaccharide, agent that causes severe nausea and reduced feeding
LiCl: lithium chloride, agent that causes severe nausea and reduced feeding
NaCh: Bacterial sodium channel, increases excitation
NPY: neuropeptide Y
NTS: nucleus of the solitary tract
Nts: neurotensin gene, neuronal cell type marker
Oxtr: oxytocin receptor gene, neuronal cell type marker
PAG: periaqueductal gray
PKC-δ+: protein kinase C, delta gene, neuronal cell type marker
PMv: ventral premammillary nucleus
POMC: proopiomelanocortin, neuronal cell type marker
PSTh: parasubthalamic nucleus
Pdyn: prodynorphin gene, neuronal cell type marker
Pnoc: Prepronociceptin, neuronal cell type marker
SCR: skin conductance response
SNc: substantia nigra pars compacta

Sst: somatostatin gene, neuronal cell type marker
Tac2: tachykinin 2 gene, neuronal cell type marker
TeLC: Tetanus toxin light chain, silences neuronal activity
US: unconditioned stimulus
VGAT: GABA transporter, most neurons in central amygdala express this
VMH: ventromedial hypothalamus
VTA: ventral tegmental area
WAT: white adipose tissue
X: 10th granial nerve
XII: 12th cranial nerve
dTa: diphtheria toxin, ablates cells that express it
eWAT: epidydimal white adipose tissue
iWAT: inguinal white adipose tissue

Chapter 1: Introduction

1.1: What is the central amygdala?

The amygdala is a crucial component of the limbic system, a network of brain structures involved in emotion and emotional responses[1]. It is well-preserved across species, from lizards to humans (see Fig. 1). Early studies have shown that the amygdala plays a significant role in fear and defensive behaviors[2,3], and extensive research has confirmed its importance in learning[1,4,5]. As a result, "amygdala fear" and "amygdala memory" are among the top amygdala-related Google searches of the past two decades[6], highlighting the prevalence with which this small brain structure is associated with these concepts. However, as the amygdala's components are studied in more varied contexts, the picture is becoming increasingly complex.

The amygdala comprises many functionally distinct nuclei and sub-nuclei, including the basolateral amygdala (BLA), which has the unique almond shape that gave the amygdala its name. The BLA can be divided into the lateral amygdala (LA) and the basal amygdala (BA), each of which has its own distinct connectivity, expression patterns, and functional roles[7,8]. The intercalated neurons (ITC), small densely packed clusters of inhibitory cells, surround the BLA[9]. The central amygdala (CeA) is located adjacent to the BLA and can be further subdivided into its lateral (CeL) and medial (CeM) parts. Each of these components have their own roles in a variety of circuits—however, this thesis will primarily focus on the central amygdala.

Previously, the CeA was considered a passive output node of the amygdala[10], using the calculations passed to it from the BLA to trigger defensive responses. Indeed, the CeA controls many aspects of fear response, such as cortisol release, increased startle responses, and regulation of the autonomic nervous system[10]. However, it is now clear that the CeA plays an active role in associative learning and in many other behaviors, including both aversive and appetitive learning, pain, addiction, feeding, and more. This thesis will broadly review what is currently known about the central amygdala and propose a novel role for the region in regulating metabolism.

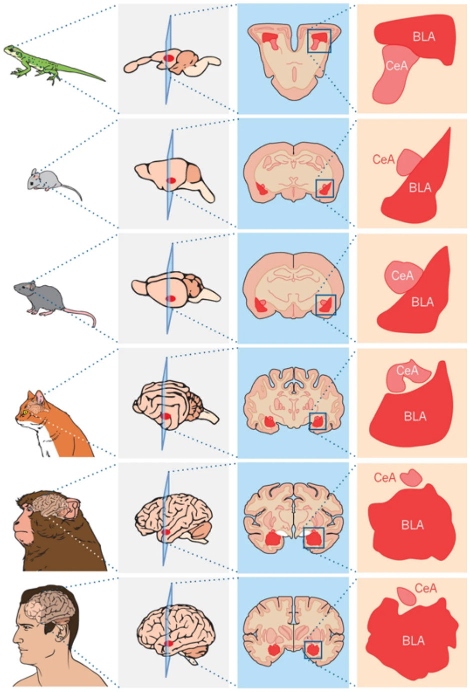

Figure 1.1: Evolution of the amygdala across species. Primary amygdalar nuclei and basic circuit connections and function are conserved across species. An enlarged image of the basolateral complex of the amygdala (BLA) and central nucleus of the amygdala (CeA) or analogues are shown next to a coronal section from the brains of a lizard, mouse, rat, cat, monkey and human. (Taken from Janak and Tye, 2015)[7].

1.2: A brief history of the CeA in fear and defensive behavior

For over 60 years, researchers have studied the amygdala in the context of fear conditioning and defensive behavior. In the 1950s, researchers observed hissing, yowling, and fleeing in cats during electrical stimulation of the amygdala[2]. In the following decades, the amygdala was studied extensively in one of the most classical types of learning—Pavlovian conditioning. In this learning paradigm, a conditioned stimulus (CS) that would normally have little behavioral significance is paired with an unconditioned stimulus (US) that has a great deal of significance. For example, a mouse that hears a 20 second sound terminating in an electric shock quickly learns to associate the sound (the CS) with the shock (the US)[11]. After successful conditioning, presentation of the CS elicits a measurable conditioned response, which can be seen behaviorally in freezing or darting, or through more general signals of alertness such as pupil dilation or skin conductance.

Individuals with amygdala damage can have deficits in recognizing emotional cues and in associative learning[12]. Human case studies have shown that amygdala damage impairs conditioned responses. In one study, a patient with bilateral amygdala damage was shown a set of monochrome slides. Blue slides were used exclusively as a visual CS and paired with an unexpected US – a 100 dB boat horn. After conditioning, control subjects showed an increased skin conductance response (SCR) in response to the blue slides. However, a patient with bilateral amygdala damage showed no increase in SCR, although he reacted strongly to the boat horn and was able to accurately describe his experiences his experiences[3]. In addition to human case studies, many early animal studies have shown the necessity of the entire amygdala in aversive conditioning[12–15].

Though these early studies shed light on the importance of the amygdala as a whole in emotional processing and associative learning, advancements in technology began to allow more targeted research on specific parts of the amygdalar circuit. Although the BLA was initially considered to be primarily responsible for integrating the stimuli required for associative learning (see Fig. 2), lesion studies demonstrated that the CeA is also necessary for learning conditioned responses[14,16,17]. With the use of in vivo brain recording techniques, researchers discovered that, like the BLA, the CeA also showed responses to CSs after learning[18–20]. They began to characterize neurons by their response profiles, identifying neurons with excitatory CS responses and neurons with inhibitory responses[21,22], with the diversity of responses hinting at a complex underlying network of activity within the CeA.

Genetic tools have since allowed for activation, inhibition, or ablation of specific populations of neurons, revealing the importance of the CeA in associative learning[23,24], and in many other types of behaviors that will be reviewed in later sections. These advances allow for more detailed study of the CeA, including cell-type specific tracing, manipulation, and recordings. Rather than being a passive node for relaying BLA output, the CeA itself experiences plasticity, and disrupting its activity during learning disrupts plasticity in the LA[24]. This evidence suggests that the amygdala may be more of a recurrent network than a linear circuit, with the CeA acting as an integral hub. We are just beginning to understand the complexity of this region and its role in behavior.

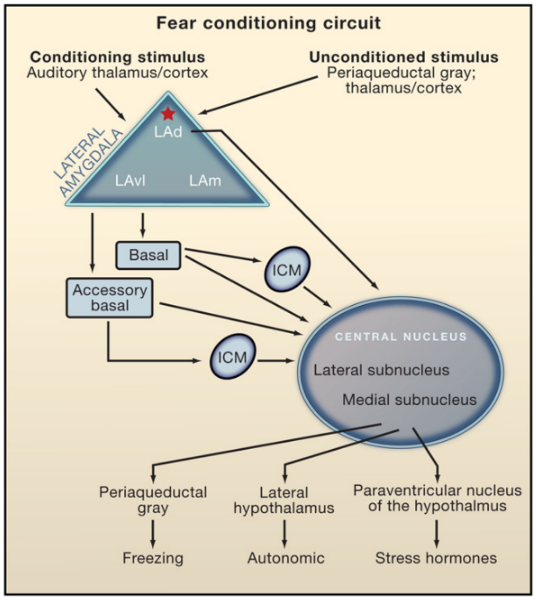

Figure 1.2. Fear Conditioning Circuit[4]. "Convergence of conditioned and unconditioned stimuli occurs in lateral nucleus of the amygdala (LA), … leading to synaptic plasticity in LA. Plasticity may also occur in the central nucleus (CE) and in the auditory thalamus. LA connects with CE directly and indirectly by way of connections in the basal (B), accessory basal (AB), and intercalated cell masses (ICM). CE connects with hypothalamic and brainstem areas that control the expression of conditioned fear responses." Taken from Johansen et. al 2011, as an example of a model of the amygdala fear conditioning circuit.

1.3: The central amygdala's projection patterns

The CeA is a highly interconnected structure, with many neurons projecting locally to other CeA neurons, forming a complex network. Additionally, the CeA receives long-range input from various brain structures, including sensory input from cortical areas such as the sensory cortex (CTXs) and insula (CTXin), as well as motivation-related input from dopaminergic areas like the substantia nigra pars compacta (SNc) and the ventral tegmental area (VTA)[25]. The CeA also receives input from other parts of the amygdalar complex, including the BLA and ITC. The CeA projects to areas that regulate the autonomic nervous system, such as the dorsal motor nucleus of the vagus (DMV), nucleus of the solitary tract (NTS), and locus coeruleus (LC), as well as to areas that control action selection, such as the periaqueductal gray (PAG), hypothalamus (HYP), and basal forebrain (BF). Some of these areas (such as SNc[19]) also have reciprocal connections to CeA. Although this is not an exhaustive list, the intricate connectivity of the CeA makes it a critical node underlying a large range of fundamental behaviors.

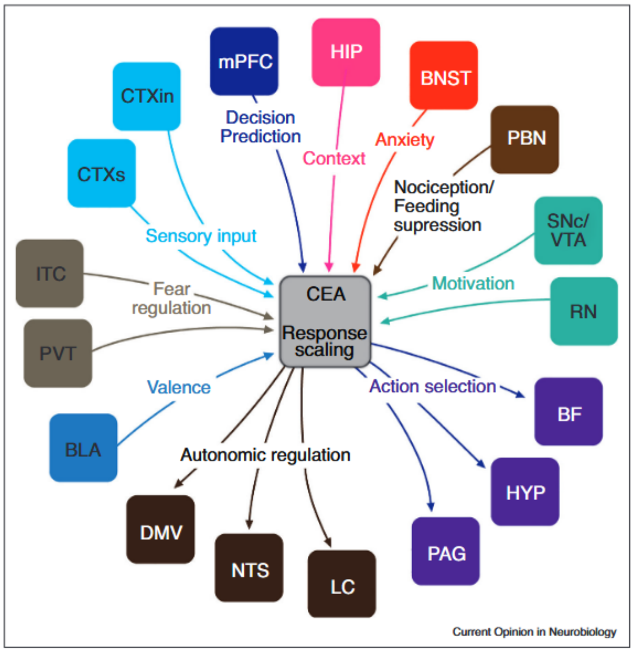

Figure 1.3: Long-range functional connectivity of the CEA. "The CEA gathers information on sensory and higher-order processes from various cortical and subcortical regions. CEA circuits mediate scaling of a complex, coordinated response transmitted through outputs that are involved in autonomic regulation and behavioral action selection."[25] (Taken from Fadok et. Al, 2018)

1.4: A broad overview of cell types and functions

In line with the complexity of the CeA's input and projection patterns, recent in situ hybridization and single-cell RNA sequencing experiments have confirmed that the CeA itself contains a diverse array of neuron types[26,27]. While most neurons in the CeA are categorized as GABAergic striatal medium spiny-like neurons[26], there are many unique cell-type markers in the CeA that have been studied, including (but not limited to) the inhibitory markers: Oxtr, CRH, Nts, Tac2, Drd2, Pdyn, Htr2a, PKC-δ+, and Sst. Each of these genetically defined populations can have diverse roles in learning and/or behavior[21,23,24,28,29]. Oxtr neurons are linked to depressive behavior after social isolation[30] and also can mediate fear responses[31,32]. CeA CRH neurons promote fear conditiong[33] and induce anxiety-like behavior through their LC projections[34]. Tac2 neurons are important for fear learning as well[35]. Pdyn neurons are important in alcohol addiction, with inhibition reducing binge drinking behavior in mice[36,37]. There is also emerging evidence that the CeA regulates feeding: Htr2a neurons promote feeding[38], while PKC-δ+ neurons (which have little overlap with Htr2a neurons) appear to inhibit it[21]. Nts neurons in the CeA promote consumption of ethanol and other palatable liquids[39], as well appetitive learning[40].

The $\text{CeA}^{\text{Sst+}}$ and $\text{CeA}^{\text{PKC-}\delta\text{+}}$ populations are frequently compared to each other because together they cover the majority of the neurons in the CeA, and they have a relatively small degree of overlap (around 10%)[29]. $\text{CeA}^{\text{PKC-}\delta\text{+}}$ neurons also directly inhibit $\text{CeA}^{\text{PKC-}\delta\text{-}}$ neurons (likely Sst+ neurons)[41]. Because of this, Sst+ and PKC-δ+ neurons are often thought of as opposing parts of a circuit. However, the reality is likely more complicated, as both groups contain mixed cell-type populations, as determined through RNA-sequencing experiments[27], and both populations serve many different functions in different contexts. Sst+ and PKC-δ+ neurons are both heavily implicated in associative learning, and both populations are needed for conditioned fear responses[23,24,41]. Sst+ and PKC-δ+ neurons also both have some evidence that they modulate anxiety[42–44], as increased activity in either population is linked to anxiety-like behavior. One study suggests these populations have opposing effects in regulating pain[45]. $\text{CeA}^{\text{PKC-}\delta\text{+}}$ neurons become sensitized by nerve injury and increase their responses to pain, while Sst+ neurons reduce their activity after injury. Activating PKC-δ+ neurons with chemogenetics worsens hypersensitivity, while activating Sst+ neurons reduces it. However, PKC-δ+ neurons may have a more complicated role in pain, as another study identified a population of neurons in the central amygdala that responds to general anesthesia that, when activated, trigger a potent analgesic effect[46]. This population shows an 80% overlap with PKC-δ+ neurons, suggesting that these neurons may contain subpopulations with vastly different roles in different contexts.

Each of the populations previously mentioned have different amounts of overlap with each other, and there have been multiple studies quantifying this[26,27]. The recent paper by O'Leary et al.[27] is an excellent reference for the cell types previously mentioned, and the authors also propose 2 novel genetically defined cell type clusters for investigation. With the diversity of cell-types represented in the CeA, more work needs to be done to understand the many roles of the CeA, as a whole.

1.5: The CeA in feeding behaviors

While there is some evidence that neurons in the CeA respond to gustatory stimuli[47] and sodium consumption[48,49], there are relatively few studies on the central amygdala's role in feeding, and fewer on metabolism. Here I will review the known populations of neurons in the CeA that respond to food or modulate feeding behavior.

The Htr2a+ neurons in the CeA respond to food and promote feeding[38]. In Douglass et. al 2017, they showed that both chemogenetic and optogenetic activation of Htr2a+ neurons robustly increase feeding in sated mice and can also counteract anorexigenic agents, including lithium chloride (LiCl) and bacterial lipopolysaccharide (LPS). Specifically ablating these neurons with diphtheria toxin (dTa) decreased feeding in fasted mice, suggesting that these neurons may be needed for feeding, or for recognizing or responding to hunger. During a free feeding assay in which they recorded single cell activity, they showed that about half of recorded neurons showed positive responses to food, with less than a quarter showing inhibition during feeding. Notably, they also confirmed that Htr2a+ neurons inhibit Htr2a- neurons locally, including some PKC-δ+ neurons.

PKC-δ+ neurons are among the populations of neurons in the CeA thought to negatively modulate feeding[21]. Cai et. al (2014) found that exposure to anorexigenic agents like cholecystokinin (CCK), LiCl, and LPS increases c-fos expression in PKC-δ+ neurons in the CeA. Further, PKC-δ+ neuron inhibition is able to completely reverse the effects of CCK on feeding in fasted animals, likely through the CeA's projection to the parasubthalamic nucleus (PSTh)[50]. PKC-δ+ inhibition also partially reversed the effects of LiCl, though not to complete recovery. In addition, optogenetic inhibition of PKC-δ+ neurons increased feeding in sated mice, and optogenetic activation decreased feeding dramatically, leading the authors to conclude that PKC-δ+ neurons may be necessary to convey a satiety signal. This study was followed by another paper showing that optogenetic stimulation of insula fibers projecting to the CeA also suppresses feeding[51], and these projections seem to target all neuron types in the CeL.

There are some limitations to this work. Although the authors concluded that CeA PKC-δ+ neuron activation with channel rhodopsin (ChR2) does not increase anxiety, in our hands it is extremely aversive[24], a factor that likely influences feeding. Also, considering the interconnected nature of the CeA and the non-uniformity of responses to stimuli (many populations, such as the previously discussed Htr2a+ neurons, have mixed positive and negative responses), ChR2 activation causes synchronous activity that is not typical of the CeA, and as a result may cause behaviors that are not typical. However, despite these limitations, newer publications that include single cell imaging make it clear that the CeA does indeed play a role in feeding, though the details still need to be worked out.

A new paper from 2022 examined the role of PKC-δ+ and Sst+ neurons in foraging and forming memories of food locations. Concurrently with the work I will present later, Ponserre et. al[52] found that PKC-δ+ and Sst+ neurons show food responses, though they report that the percentage of food-responding neurons is higher in Sst+ neurons than in PKC-δ+ neurons. The authors inhibited each of these populations during a free-moving feeding task, in which they conditioned mice to expect food at a specific location. Inhibition of PKC-δ+ neurons during conditioning impaired learning of food locations, while Sst+ neuron inhibition did not. PKC-δ+ neuron inhibition during recall also impaired conditioned food responses. Single cell imaging revealed a population of PKC-δ+ neurons that activated when mice approached the conditioned food locations. The authors conclude that PKC-δ+ neurons may help mice form memories of foraging locations, potentially by linking the salience or valence of the food stimuli to the context in which the food is found. Although this work, like much of the former feeding related literature, focuses on the CeA's role in feeding through the lens of learning and memory, it is among the first to show that PKC-δ+ and Sst+ neurons respond to food.

The CeA is also integral for hunting behavior in mice[53]. Han et. al show that 2 separate projections of GABA transporter (VGAT) expressing neurons in the CeA (mainly in the CeM) are responsible for distinct hunting behaviors- prey pursuit and prey attack. They showed that the CeA's projections to the reticular formation are necessary for coordinating the neck and jaw muscles needed for effectively dispatching prey, and stimulating these projections with ChR2 results in coordinated movement of the masseter and trapezius muscles. In contrast, CeA to PAG projections are needed for prey pursuit, and disrupting this pathway increases the amount of time it takes mice to catch their prey. They also recorded in vivo activity from neurons in the CeA using electrode arrays, demonstrating that a large proportion of recorded neurons responded to components of hunting behavior.

There is also some limited information suggesting that the CeA may play a role in metabolism. One of the papers to touch on this studied the role of Prepronociceptin-expressing (Pnoc+) neurons in the CeA[54]. They found that ablation of these neurons with caspase reduced consumption of a palatable high fat diet (HFD), and this manipulation slightly reduced weight gain over 9 weeks on HFD, likely through reducing the amount consumed. These effects on feeding were specific for HFD, and the ablation also disrupted preference formation. Chemogenetic inhibition also reduced consumption of HFD but not normal chow, and excitation of CeA Pnoc+ fibers in downstream regions (NTS, BNST, and PBN) was positively reinforcing, suggesting that Pnoc+ neurons in the CeA may modulate the hedonic aspects of feeding and may perhaps play a role in obesity through overconsumption of HFD.

There are hints of metabolic effects from this manipulation, such as a reduced RER and body temperature in mice fed HFD with Pnoc+ neuron ablation, though it's unclear whether these effects are mediated simply by less consumption of HFD, and the study does not further explore this. Mounting evidence is beginning to suggest that the CeA could be involved in energy homeostasis, and can potentially combat weight gain on a high fat diet through increasing sympathetic innervation of adipose tissue[55]. Additionally, somatosensory innervation of adipose tissue also plays an important role in regulating metabolism[56], and it is unknown which brain areas may contribute to this modulation.

Although much of the literature around the CeA focuses on learning, these studies report that the CeA displays significant food responses and can modulate feeding behavior, hunting, food memory, and potentially metabolism. However, despite the increasingly recognized role of the CeA in feeding, there is still very little information about how CeA neurons respond to different foods during feeding, whether changes in body weight affect food responses, or whether disrupting CeA activity changes how food is processed outside of the brain. To my knowledge, there are no studies that clearly link in vivo activity in the CeA directly to metabolism.

1.6: Feeding circuits in the brain

With the emergence of the CeA as a key player in feeding, it is important to consider the well-established feeding circuits throughout the brain, and how the CeA may fit into these circuits. Among the most well-known hubs for modulating appetite is the hypothalamic arcuate nucleus (ARC, see fig. 1.6), which contains 2 interspersed populations with opposing effects on feeding behavior[57]. These populations are Agouti-related protein (AGRP)-expressing neurons and proopiomelanocortin (POMC)-expressing neurons. AGRP+ neurons increase their activity before a meal, then decrease their activity during feeding. Stimulation of these neurons leads to robust feeding behavior and increases the amount of effort that mice will expend to access food, whereas ablation in adult mice can lead to starvation. AGRP+ neurons release GABA, as well as the neuromodulators AGRP and NPY, which increase feeding when injected into the brain. These neurons are also responsive to circulating feeding-related hormones, including ghrelin, which is synthesized in the gut and promotes feeding, and leptin, which is released by adipose and can signal satiety. AGRP+ neurons target many downstream brain regions, some of which can also trigger feeding. These areas include the PVH, BNST, LH, and PVT. Together, these observations have led to the current consensus that AGRP neurons signal hunger and promote motivation to seek out food.

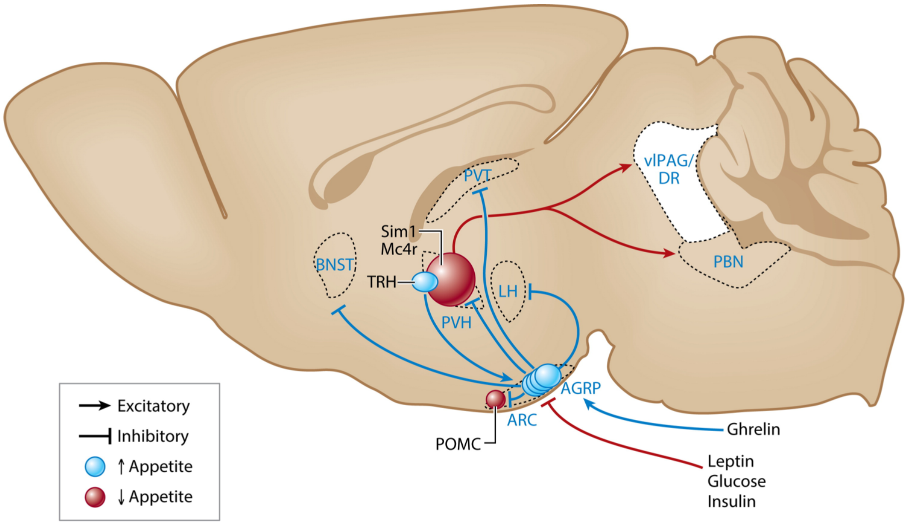

Figure 1.6: Summary diagram illustrating AGRP neuron circuits that influence food consumption. "Inhibitory AGRP neuron projection fields whose activation is sufficient to induce food consumption behaviors: the PVH, BNST, LH, and to a lesser extent, the PVT." Taken from Sternson et. al, 2017.

Sternson SM, Eiselt A-K. 2017.
Annu. Rev. Physiol. 79:401–23

The counterpoint to the AGRP+ neurons in the ARC are the POMC+ neurons[58]. These leptin-sensitive neurons inhibit feeding during satiety. Activation of these neurons prevents feeding. Other regions of the hypothalamus express functional receptors for leptin, including the dorsomedial (DMH), ventromedial (VMH), and lateral (LH) parts, as well as the ventral premammillary (PMv) nuclei[59]. The PAG and brainstem nuclei, like the NTS and DMV, can also respond to leptin, and the VTA expresses leptin receptors in a subset of its dopaminergic neurons.

The dopamine reward system is also an integral part of feeding[60,61], and dopamine neurons in the VTA play a role in food-seeking and food-anticipatory behavior, and in responding to food cues, such as the sight and smell of food. The VTA also receives dense projections from the LH, and stimulation of these projections is sufficient to drive feeding behavior[62]. This mesolimbic dopamine signaling is thought to be important for the motivation to earn food rewards, though food consumption can also be mediated through SNc to DS nigrostriatal pathways. Thus, feeding and food anticipation are mediated by the interplay of both the dopamine reward system circuits and by hypothalamic feeding circuits.

The CeA interacts with many nodes in these circuits. The CeA receives reciprocal input from the VTA, as well as the SNc, and there is some evidence that SNc-projecting neurons from the CeA may be involved in processing food-predicting cues[19]. The CeA also projects to the NTS, a major sensory nucleus that receives visceral information from the periphery, including feeding related signals such as stomach and intestine stretch after a meal[63]. The CeA also receives input from the NTS and PBN, and sends projections to the PSTh, a small nucleus in the posterior part of the LHA. Although there is still much left to untangle, the CeA interacts with multiple essential feeding and homeostatic circuits.

1.7: A broad overview of feeding in the rest of the body

Although the topic is much too expansive to fully cover here, I will outline some of the main ways that the body processes food, focusing on fat, and highlight the most integral organ systems (see fig. 1.7a).

The first step in digestion is to consume food. After being roughly broken down in the mouth, food is swallowed and pushed towards the stomach through the esophagus. After passing into the stomach, food is then further broken down, both mechanically and chemically, with various enzymes and the assistance of a low Ph environment[64]. Over several hours following the meal, the stomach slowly empties into the duodenum, the first part of the small intestine, where enzymes from the pancreas work to break down fats, proteins, and carbohydrates. The pancreas also secretes insulin, a hormone which helps glucose enter cells to be used as fuel. Bile acids secreted from the gallbladder aid in digestion by working to emulsify fats. Food is moved down the small intestine, and in the ileum and jejunum, broken down material is absorbed into the veins surrounding the intestine, called the hepatic portal system. Any undigested material (like fiber) travels into the large intestine, where water is further removed and bacteria can participate in digestion, before being excreted from the body.

During this complex process, fats are broken down, then taken up into the cells of the intestine. There, some types of fat are packaged and excreted into lymphatic vessels, and soluble fatty acids (FAs) are able to enter the portal vein and be transported to the liver. The liver can then distribute these fatty acids for fuel during an energy deficit, or help store the fat in adipose tisue[65]. The liver is also very important in processing carbohydrates, and it can help distribute them as fuel to the periphery, or store some sugars as glycogen as an energy reserve.

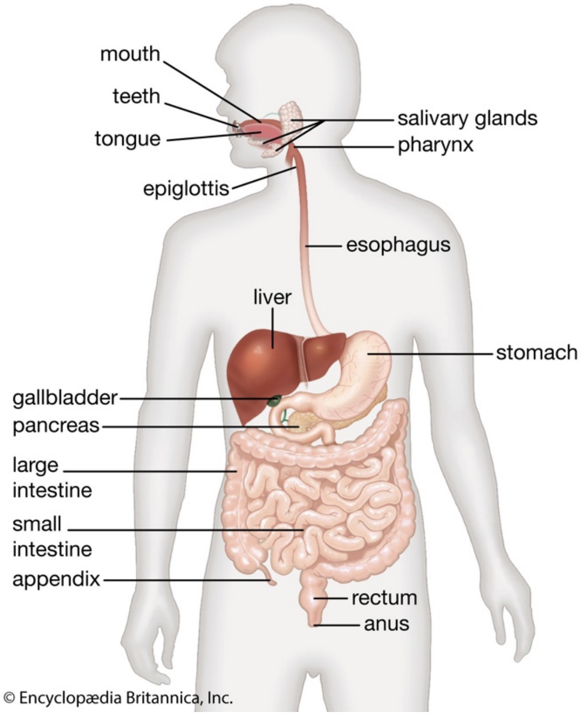

© Encyclopædia Britannica, Inc.

Figure 1.7a: Key organs in digestion, from the Encyclopedia Britannica, Inc.

Most reserved energy is stored in white adipose tissue (WAT) in adipocytes as triglycerides (TGs)[66]. These are made in adipocytes by taking up fatty acids (FA) circulating in the blood and converting them to TGs through the actions of a complex interplay of enzymes. In a state of metabolic dysfunction, such as in obesity, adipose tissue can expand through an increase in the size of adipocytes, or through formation of new adipocytes (called adipogenesis)[67]. It is also possible for the liver and white adipose to synthesize TGs through lipogenesis of non-fatty acids, though this may not be as common in humans as in small mammals. To access energy stores from adipocytes, and TGs must be broken down into FAs once again (a process called lipolysis), then transported to plasma. Adipose tissue can also secrete hormones[68] like leptin, which affect satiety by acting on the brain. There is also an intricate interplay between adipose and the immune system[69] that should be mentioned, though this thesis will focus only on metabolism and feeding.

Sympathetic innervation plays an integral part in fat metabolism[70], and the satiety-regulating circuits discussed previously, including hormone-sensitive neurons in the ARC, connect to presympathetic neurons in the spinal cord, which in turn regulate sympathetic tone of adipose tissue[70] (see fig. 1.7b). Adipocytes express multiple types of adrenergic receptors, and sympathetic tone can influence lipolysis and induce thermogenesis in brown adipocytes, a process that expends energy and is important for regulating temperature. Parasympathetic innervation of adipose tissue, especially WAT, has been hotly debated over the past 20 years, but recent 3D imaging studies of WAT conclude that there are few parasympathetic fibers innervating this tissue, compared to sympathetic innervation[71]. Interestingly, WAT does receive somatosensory innervation that may work as a feedback system for the brain to counterbalance the effects of sympathetic input[56]. This, together with the brain's ability to sense hormones excreted from adipose, forms a brain-adipose loop that has important implications in how adiposity is controlled.

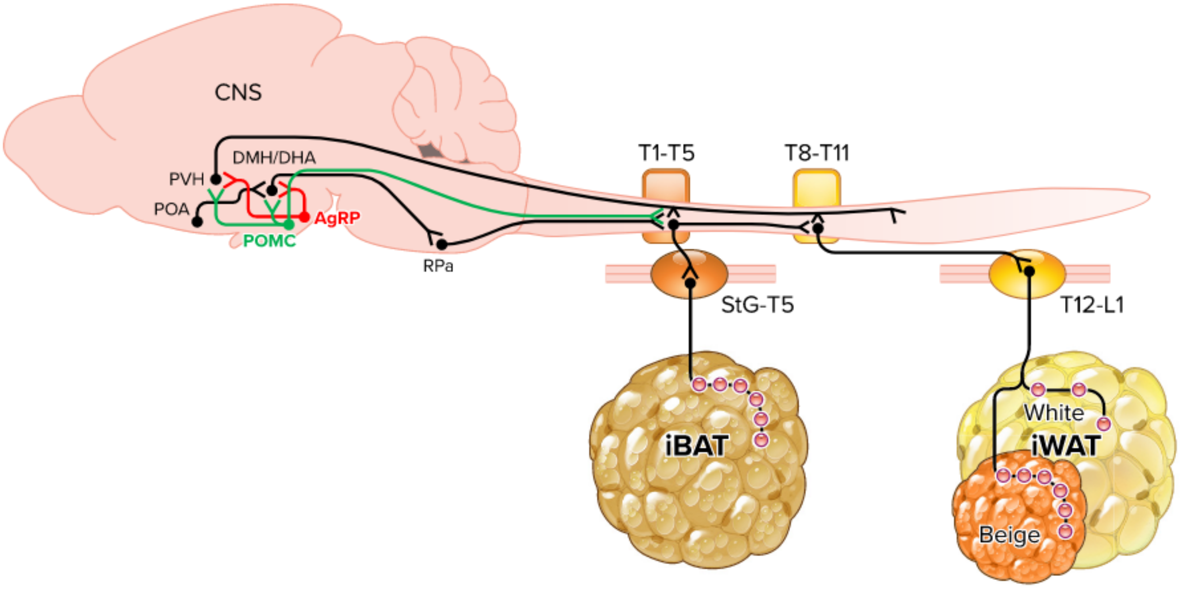

Figure 1.7b. Adipose tissue innervation scheme. "This scheme highlights the emerging concept of differential sympathetic tone and innervation density in select adipose tissue depots [e.g., interscapular brown adipose tissue (iBAT) and inguinal white adipose tissue (iWAT). Brain circuits connect neurons either directly (e.g., POMC,PVN,and RPa neurons) or indirectly (e.g., POA, DMH/DHA, POMC, and AgRP neurons) with presympathetic neurons in the spinal cord. POA, preoptic area; PVH, paraventricular hypothalamus; DMH/DHA, dorsomedial hypothalamus/dorsal hypothalamic area; POMC, pro-opiomelanocortin; AgRP, agouti-related peptide; RPa, raphe pallidus; StG, stellate ganglion; T, thoracic level; IML, intermediolateral bundle; NE, norepinephrine". Taken from Munzberg et al., 2021

1.8: The rise of obesity and related health risks

Elucidating the role of the brain in feeding and metabolism and its interaction with adipose tissue is more urgent than ever, as the rates of obesity continue to rise[72–74]. High-income economy countries lead this trend, though many countries with middle or low-income economies are beginning to show increases in obesity as well[75]. Though many factors affect health and not all obese individuals appear to be metabolically unhealthy[73,76], obesity is associated with a decrease in lifespan[77–79] and is often comorbid with a number of diseases. These include type 2 diabetes[80], fatty liver disease, cardiovascular diseases (stroke, heart attack, high blood pressure), arthritis, depression, and cancer[79].

Attempts to lose weight often fail, as weight loss induces metabolic adaptations that seem to promote weight regain[81–83]. One of the most extreme examples of this are the longitudinal studies of participants from the American TV show, "The Biggest Loser," a show in which participants compete to lose the highest percentage of body weight over the course of the television season[81,82]. These studies follow the "Biggest Loser" participants (BLPs) who experienced massive weight loss through caloric restriction and exercise and compared them to people who underwent bariatric surgery to lose a similar amount of weight. The BLPs were much more likely to regain the weight they lost compared to the group with surgical intervention, and they experienced persistent metabolic adaptations that likely promoted their weight regain. Although the rate of weight loss in BLPs was unusually swift (and the weight loss methods too extreme to be considered safe, by some), these studies demonstrate how weight loss can be fiercely counterbalanced by metabolic adaptations that encourage the weight to return. The mechanisms behind this are not understood, and currently the most effective long term weight loss treatment is gastric bypass surgery.

Unfortunately, there are many risks associated with bariatric surgery, including vitamin deficiencies, severe reductions in bone density, and gastroesophageal reflux disorder (GERD)[84,85]. There are promising new drugs that target the glucagon-like peptide (GLP-1) receptor that seem to be effective in causing weight loss and improvement of metabolic disorders, likely through targeting both the nervous system and also the insulin secreting B cells of the pancreas[86–88]. Adipose tissue also expresses GLP-1 receptor, and there is some evidence that treatment with an agonist can improve insulin resistance in adipocytes, as well[89]. However, these drugs, too, cause many undesirable side effects ranging from nausea and dizziness to thyroid tumors. Additionally, it is not clear yet how long patients need to maintain use of these drugs in order to avoid weight regain. There is still a clear need for better obesity treatment, and for better understanding of the interplay between the brain, the body, and metabolism.

Chapter 2: A new role for the central amygdala PKC-δ+ neurons in metabolism

2.1: Introduction

Foods high in fat and sugar are increasing in prevalence, with many middle- or high-income countries blowing past the recommended nutritional levels[90,91]. In parallel, metabolic disorders, such as obesity and diabetes[80,92], are becoming much more common globally. Current interventions for obesity often fail, as weight loss induces metabolic adaptations that promote weight regain[81-83]. Therefore, it is becoming increasingly more urgent to understand the metabolic processes that go awry during obesity. The brain can monitor feeding by integrating sensory information (taste, odor, texture, etc.) with consummatory signals from the periphery[56,63,88,93], and it can direct feeding through a variety of circuits (see chapter 1.6). It also modulates metabolism by influencing peripheral organs, such as intestine and adipose tissue[70,88,94,95]. However, the link between the brain's activity during food consumption and downstream metabolic processes such as weight-gain, fat deposition, and energy expenditure is unclear.

Here, we propose a nuanced role for PKC-δ+ CeA neurons ($\mathrm{CeA}^{\mathrm{PKC\text{-}\delta+}}$) in metabolism. There is an evolving role for the CeA in feeding (see chapter 1.5), and the prevailing view is that $\mathrm{CeA}^{\mathrm{PKC\text{-}\delta+}}$ neurons act as appetite suppressors[21]. However, to our knowledge, there has been no investigation of how internal hunger state (i.e. caloric restriction vs. excess caloric consumption) affects CeA$^{PKC\text{-}\delta+}$ neuron activity. We demonstrate that these neurons are able to encode and distinguish between nutritionally relevant gustatory stimuli. These responses are present regardless of internal hunger state of the animal, though exposure to a high fat diet and the resulting weight gain can fundamentally alter food responses and increase baseline activity of CeA$^{PKC\text{-}\delta+}$ neurons. We then translate our observations into functional manipulations of CeA$^{PKC\text{-}\delta+}$ neurons to demonstrate a previously unknown role for these neurons in regulating weight-gain and metabolism.

2.2: CeA$^{PKC\text{-}\delta+}$ neurons have robust photometry responses to food, regardless of hunger or preference

CeA$^{PKC\text{-}\delta+}$ neurons are almost exclusively studied for their role in feeding suppression and satiety[21,50,51], but currently there are no reports closely examining *in vivo* activity during feeding to corroborate this. To investigate how these neurons respond during a meal, we prepared PKC-δ-Flp-2A mice for photometry[96–98] by injecting a viral vector expressing Flp-dependent gCaMP6m into the CeA, then implanted an optic fiber over the same area to record bulk CeA$^{PKC\text{-}\delta+}$ responses during feeding behavior (Figure 1q). As these neurons are believed to suppress feeding during satiety, we first recorded the CeA$^{PKC\text{-}\delta+}$ neuron activity in sated mice while presenting an appetitive stimulus (white chocolate) to drive hedonic consumption (Fig. 1a-f).

For each trial, we used a 2-chamber system to place a piece of chocolate in a main chamber, then lifted a removable door to allow mice to approach and consume the chocolate while recording photometry responses (Fig. 1a). Strikingly, each eating bout led to a large increase in CeA$^{PKC\text{-}\delta+}$ neuron activity that lasted the entire duration of the bout, usually lasting over 30 seconds and then decreasing back to baseline after the cessation of feeding (Fig. 1b-d). Inedible objects, such as similarly sized pieces of eraser, did not elicit any response during gnawing behavior (not shown). There was no correlation between the length of the bout and the peak of the response and no clear difference between the first bout and the last (Fig. 1e,f). The constancy and duration of the signal was unexpected, and it does not seem to vary with increasing satiety.

Considering the unexpected nature of these responses, we next sought to examine food responses throughout different hunger states in a more controlled way. As the 2 largest nutritional components of white chocolate are fat and sugar, we custom-ordered 2 different 20 mg pellets with either high fat (HF, ~27% fat by caloric content) or high sucrose (S, 95% carbohydrates, by caloric content), then used an automated feeding device (FED3[99]) to randomly dispense the pellets during photometry recordings (Figure 1g-k). In sated mice, we saw responses to both pellets that lasted the duration of the feeding bouts, ~20-30 seconds, with little difference between the two (Figure 1h-i). Mice under food-restriction showed very similar responses to both pellets, indicating that CeA$^{PKC\text{-}\delta+}$ neurons are likely not exclusively conveying satiety, as previously suggested. Indeed, we saw responses to every type of food the mice consumed while food-restricted, including their regular diet, dark chocolate, and various flavored diets (not shown). To exclude the possibility that these neurons were simply responding to the process of eating, we used a liquid delivery experiment to alter the tactile and motor experience of consuming fat and sugar.

We delivered isocaloric solutions of fat and sucrose in randomly interspersed trials through 2 nearby but separate spouts (Figure 1l). Each trial lasted until mice voluntarily approached and licked the active spout. In mice that were not thirsty (quenched), both the fat and the sucrose solution elicited consistent responses (Figure 1m). Most quenched mice licked more vigorously to the sucrose solution, indicating a clear preference for sucrose (Figure 1n, left). However, fat responses were consistently larger than sucrose responses, regardless of preference (Figure 1n, right). Under water-restriction, the difference between fat and sucrose responses becomes clearer (Figure 1o-p), and fat responses remain larger than sucrose responses, despite a reversal in preference. This data suggests that PKC-δ+ neurons in the CeA can respond to various foods (and caloric liquids) regardless of internal state and maintain these responses independently of preference. However, as photometry is a method for recording bulk activity, it does not capture the nuance of single cell responses. More resolution is needed to capture the full possible range of CeA$^{\text{PKC-}\delta+}$ responses.

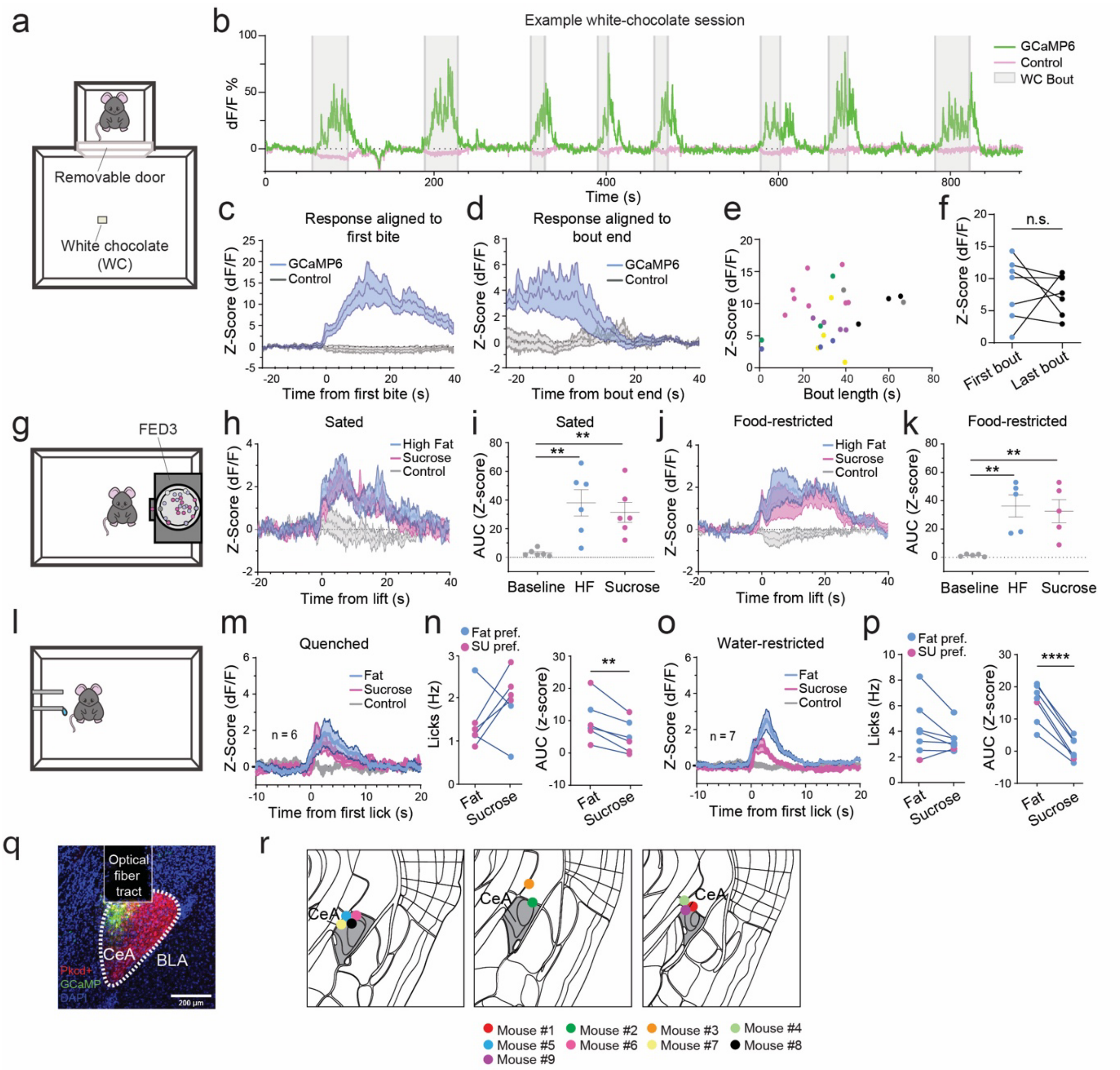

Figure 1: Photometry responses of PKC-δ+ neurons to fat and sugar in different forms

A. Experimental setup for free-moving feeding assay. **B.** Example full session photometry trace from a representative mouse. **C.** Average z-score response plotted with the isosbestic control channel, with time 0 aligned to the first bite (n = 7). **D.** Average z-score with time 0 aligned to the time the mouse ends feeding bout (n = 7). **E.** Peak z-score vs eating bout length. No correlation (Pearson correlation, p = 0.2254, n = 7 mice). **F.** Peak z-score of first and last bout (paired t-test, p = 0.576, n = 7 mice). **G.** Diagram of free-moving FED3 feeding experiments. **H.** Average z-score of sated responses to each pellet type, aligned to pellet pickup (n = 5). **I.** Average AUC of sated pellet responses compared to 10 seconds before pellet approach (2-way ANOVA, then Sidak's test: p = 0.0015, 0.0060, n = 5). **J.** Average z-score of food-restricted responses to each pellet type, aligned to pellet pickup (n = 5). **K.** Average AUC of food-restricted pellet responses compared to 10 seconds before pellet approach (2-way ANOVA, then Sidak's test: p = 0.0024, p = 0.0048, n = 5). **L.** Diagram of 2-Spout Task, where isocaloric solutions of fat and sucrose are dispensed from 2 different

Figure 1 (continued): spouts. **M.** Average z-score of responses to fat and sucrose in non-thirsty mice, n = 6. **N.** Average spout licks for each liquid, coded by preference (left) and average liquid responses in sated mice (right, paired t-test: $p = 0.0033$, $n = 6$). **O.** Average z-score of the water-restricted responses to fat and sucrose. **P.** Average spout licks in response to each liquid, coded by preference (left) and AUC of the z-scored responses to each liquid (right, paired t-test: $p = 0.00005$, $n = 7$).

2.3: CeA$^{PKC\text{-}\delta+}$ neurons represent food-related stimulus qualities

Next, to gain more resolution into the function of CeA$^{PKC\text{-}\delta+}$ neurons, we imaged their responses to various stimuli at single-cell resolution. To this end, we targeted expression of GCaMP6 to CeA$^{PKC\text{-}\delta+}$ neurons and implanted a gradient-index (GRIN) lens above the CeA. Using a one-photon wide-field microscope, we imaged the GCaMP6 signal in individual CeA$^{PKC\text{-}\delta+}$ neurons through the GRIN lens[96,97,100] while presenting a panel of liquid stimuli to water-restricted mice under head restraint, using a 6-spout delivery system (Fig. 2a; Methods). As our initial photometry experiments demonstrate strong responses to fat and sucrose, we included these stimuli to investigate whether CeA$^{PKC\text{-}\delta+}$ neurons can distinguish between them by taste, or respond in a general way to any caloric stimuli. Fat and sugar can be directly detected in the mouth (as well as post-ingestively by the gut[101]) and early literature suggests texture is also a key component of fat detection and food pleasantness[102]. As such, to investigate whether stimulus texture or "mouthfeel" can be represented by CeA$^{PKC\text{-}\delta+}$ neurons, we included stimuli that typically signal caloric density (i.e. viscosity and oiliness).

To this end, we chose mineral oil, a non-caloric viscous liquid with an oily texture, and 0.1% xanthan gum, a tasteless thickener chosen for similar viscosity[103,104] but without an oily texture. Additionally, as CeA$^{PKC\text{-}\delta+}$ neurons are known to respond to negative stimuli[24], we also included a quinine solution and air puff, two aversive stimuli across distinct sensory modalities. Water was also given for comparison and delivered between imaging trials to ensure no residue from previous stimuli remained. All stimuli were randomly interspersed, with any excess fluid vacuumed away at the end of each trial. This panel of stimuli captures important properties of highly caloric foods, including fat and sugar content, texture, taste, and valence.

Interestingly, each of these stimuli evoked robust responses in some CeA$^{\text{PKC-}\delta+}$ neurons, with most of the stimuli selectively activating or inhibiting distinct subpopulations (Fig. 3a, see Fig. 2c for example neuron responses). Some neurons showed preferential responses towards specific stimuli, demonstrating that CeA$^{\text{PKC-}\delta+}$ neuron activity reflects differences in the stimuli rather than general motor programs for drinking. To get an idea of underlying structure or patterns in these responses, we used K-means clustering of individual neuronal response profiles to these stimuli to reveal nine clusters (C1-C9; Fig. 3a,b): two clusters (C1 & C7) mainly respond to air puff, one (C4) responds in an excitatory way to all liquids but shows inhibition to air puff, two (C2 & C3) show responses to mineral oil, one (C5) shows a large response to quinine, one (C8) shows inhibitory responses to all stimuli, one (C9) shows little response to any stimuli, and one (C6) responds mainly to fat and sucrose, the only caloric stimuli presented. There were no clusters grouping quinine and air puff together (the negative valence stimuli), as we originally suspected.

To examine how the CeA$^{\text{PKC-}\delta+}$ neurons represent the relationships between these stimuli, we constructed a correlation matrix of all stimulus pairs using Pearson correlation coefficients calculated based on each neuron's responses (Figure 3c). Then, using these coefficients as a distance metric, we hierarchically classified the stimuli. The most closely related stimuli were water and xanthan gum, suggesting that viscosity alone is not encoded by these neurons. Fat and sucrose were also closely linked, perhaps because they were both caloric. Mineral oil was the liquid that was most distinct from the other liquid stimuli, and indeed, it was qualitatively the oiliest of these stimuli. Surprisingly, quinine was clustered closest to water and xanthan gum, despite its bitter nature. In contrast, air puff – the other stimulus with a negative valence but different sensory modality – was classified as the most distant stimulus. These results suggest that CeA$^{PKC\text{-}\delta+}$ neuron activity may distinguish between these stimuli according to a hierarchy of stimulus qualities, including sensory modality (i.e. air puff vs. all other stimuli), chemical properties/texture (oiliness of the mineral oil vs. the other liquids), and caloric content (fat or sucrose vs. non-nutritious liquids), with less emphasis placed on valence than expected.

To further examine how CeA$^{PKC\text{-}\delta+}$ neurons represent these stimuli, we performed t-distributed stochastic neighbor embedding (t-SNE) using 20 single-trial responses for each stimulus, combining the single-neuron responses from all mice. Each stimulus was easily separable in the t-SNE space, except for water and xanthan gum (Fig. 3d). We then built a linear classifier and tested it using 5-fold cross validation over different t-SNE constructions to achieve an overall accuracy of 90.71%. To visualize the most likely trials to fail in classification, we used a representative t-SNE plot, trained a linear classifier, and predicted class labels for the dataset (with resubstitution), marking the misclassified trials with an X, as a method to evaluate classifier performance specific stimuli. The classifier had the lowest performance in distinguishing between water and xanthan gum, consistent with them being "closest" among all the stimuli. Moreover, xanthan gum and water elicited similar responses, despite the fact that the former has a much higher viscosity and often triggers higher lick rates (Figure 2d). Altogether, these results suggest that CeA$^{PKC\text{-}\delta+}$ neurons have the capacity to represent many qualities of a stimulus, including its sensory modality, texture (but not viscosity), taste, and potentially caloric content.

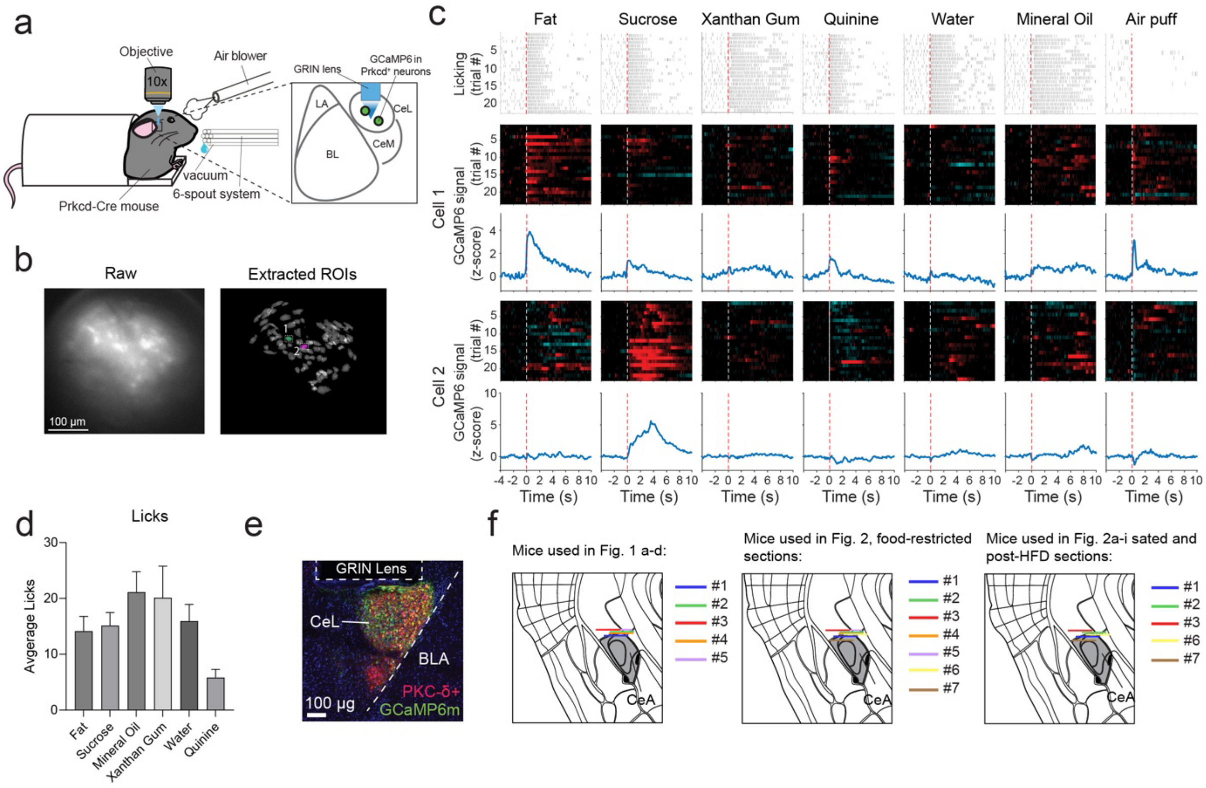

Figure 2: Experimental setup for CeA$^{PKC\text{-}\delta+}$ liquid imaging experiments

A. Setup for 1-photon GRIN lens liquid and air puff experiments. Mice are head-fixed and randomly given 6 different liquid stimuli and air puffs, interspersed. **B.** Example raw imaging data (left) and the extracted single neuron ROIs (right). 2 example neurons are selected and highlighted from the ROIs. **C.** Traces from the 2 example neurons. Top: raster plots of all spout licks during each trial type, aligned to the first lick. Middle: heatmaps show individual trial signal (Z-score of dF/F). Bottom: Average traces aligned to time of first lick. **D.** Histology from a representative mouse. **E.** Histology of mice used in all experiments.

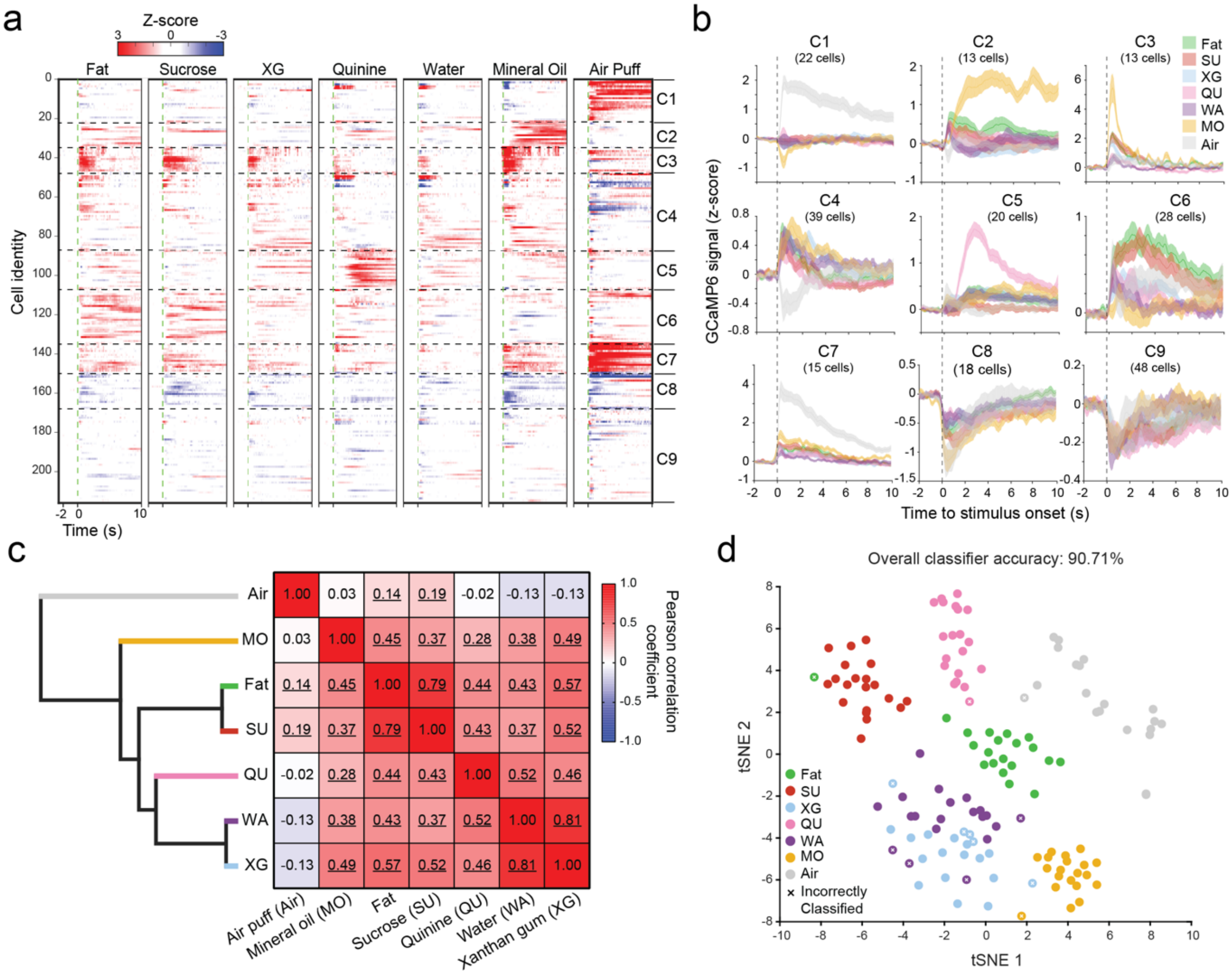

Figure 3: $\text{CeA}^{\text{PKC-}\delta+}$ neurons are able to encode and distinguish a large variety of gustatory stimuli. A. Clustering of average single neuron responses for each liquid (270 neurons across 6 mice). Clustering was performed using k nearest neighbors after using a Silhouette test to determine appropriate number of clusters. **B.** Average responses from each cluster to each liquid and air puff. **C.** Correlation matrix of each stimulus calculated using all neural responses (Pearson). Significant correlations are underlined. Stimuli were then clustered hierarchically using the Pearson correlation between stimulus pairs as a distance metric. **D.** t-SNE plot of 140 recorded trials across 5 mice (270 neurons). Trained a linear discriminant classifier, first on the training set with resubstitution to highlight trials that fail to be classified (marked with an x), then with 5-fold cross-validation to estimate the accuracy of the model (90.71% accuracy).

2.4: CeA$^{PKC-\delta+}$ neurons can encode nutritional differences across both food-restriction and satiety

We established that CeA$^{PKC-\delta+}$ neurons can encode some relevant nutritional properties, so we next sought to characterize their responses to highly caloric foods across different metabolic states. These neurons were considered anorexigenic and thought to signal satiety, so we selected appetitive food stimuli to compare responses between mice that were first food-restricted, sated, and then fed a high fat diet (HFD) for a period of 2-3 weeks. We used the same appetitive pellets used in the photometry experiments: high-fat and high-sucrose pellets. We delivered the different pellets (20 mg/pellet) to head-restrained mice in a random order using a modified FED3 device while imaging CeA$^{PKC-\delta+}$ single neuron activity (see Fig. 5a for experimental setup). The device failed to dispense pellets on a small number of trials, in which the FED3 motor turned (and made the same noise as in other trials) but no pellet was delivered. These "miss" trials serve as a convenient control in which mice expect to receive food but do not.

In food-restricted mice, we found that many neurons were excited by either or both pellets and displayed robust, long-lasting responses during feeding (Fig. 4a). Similarly, many neurons also displayed long-lasting inhibitory responses. Interestingly, although many neurons responded similarly to both pellets, neurons often displayed pellet-specific responses (Fig. 5d). Some neurons also displayed responses to the sound of the FED3 motor during missed trials, though these responses were brief and weak compared to the responses in food delivery trials. Imaging in sated mice returned broadly similar results. In fact, we were able to track a subset of food-responding neurons across food-restricted and sated imaging sessions (see example neurons in Fig. 5b-c) with some displaying consistent responses to one or both types of pellets. These results are consistent with the photometry data, demonstrating that CeA$^{\text{PKC-}\delta+}$ neurons strongly respond to food in both hungry and sated contexts and do not appear to exclusively signal satiety.

To assess whether CeA$^{\text{PKC-}\delta+}$ neurons can distinguish between the high-fat pellets and the high-sucrose pellets, we first used principal component analysis (PCA) on all recorded single neuron average responses to reduce the dimensionality and visualize the food responses (Fig. 4b). Notably, the trajectories of the average pellet responses from both food-restricted and sated mice were clearly separable according to pellet type. Furthermore, we trained a support vector machine (SVM) classifier for the two types of pellets using the responses from each mouse, and we found that pellet identity could be predicted with high accuracy, for either food-restricted (90%, Fig. 4c, left) or sated (97%, Fig. 4c, right) mice. Thus, different types of food are uniquely encoded by CeA$^{\text{PKC-}\delta+}$ neuron activity across different hunger states, and it is likely that these neurons signal the taste or the nutritional makeup (i.e., fat vs. sugar) of these pellets.

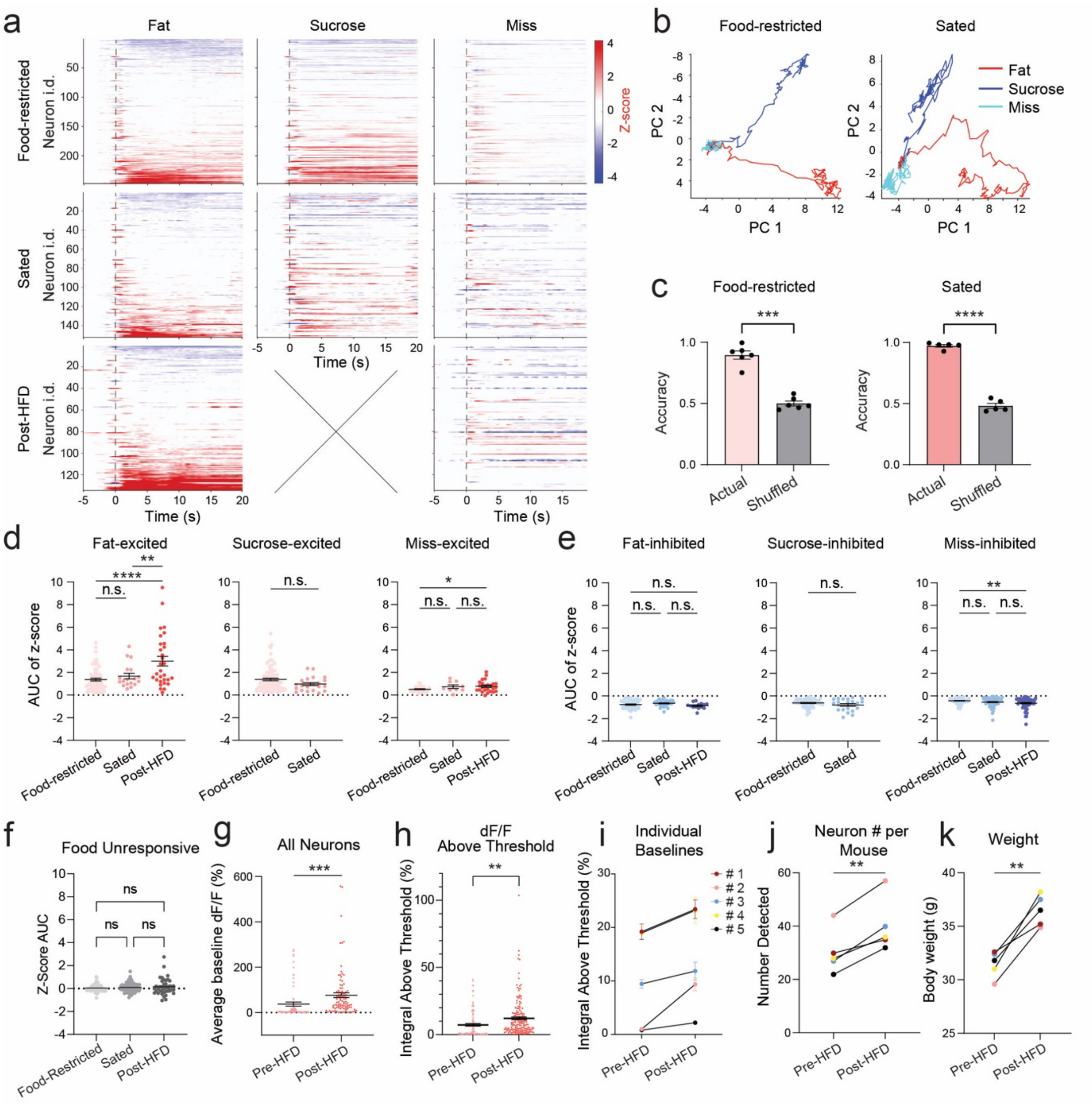

Figure 4: CeA$^{PKC\text{-}\delta+}$ neurons respond robustly to high fat and high sucrose foods and can distinguish between them, regardless of internal hunger state

A Heatmaps of average single neuron responses during food-restricted, sated, or post-HFD imaging sessions. Sucrose trials are excluded from post-HFD data due to low trial numbers. **B.** PCA of food-restricted and sated data from the same representative mouse, using average single neuron responses over a 15 second time period, beginning 3 seconds before food contact (3 seconds before motor turn for missed trials). The beginning of each trace is marked by a star. **C.** SVM classifier accuracy in food-restricted sessions (90% accuracy, n = 6, paired t-test, $p = 0.0004$) or sated sessions (97% accuracy, n = 5, paired t-test, $p < 0.0001$). The “actual” classifier was trained and tested on subsets of high fat and high sucrose pellet trials, and the “shuffled” classifier was trained and tested on trials with randomly shuffled

Figure 4 (continued): PKC-δ+ neurons respond robustly to high fat and high sucrose foods and can distinguish between them, regardless of internal hunger state

labels. Each mouse was separately used to train classifiers. **D.** Average area under the curve (AUC) Z-score responses of neurons with significantly positive responses, flagged using permutation tests (Fat-excited: FR vs S $p = 0.7084$, FR vs. pHFD $p < 0.0001$, S vs. PHFD $p = 0.0093$. Sucrose-excited: FR vs S $p = 0.0987$. Miss-excited: FR vs. S $p = 0.2616$, FR vs. pHFD $p = 0.0361$, S vs. pHFD $p = 0.9781$) **E.** Average area under the curve (AUC) Z-score responses of neurons with significantly negative responses, flagged using permutation tests (Fat-inhibited: FR vs S $p = 0.3317$, FR vs. pHFD $p = 0.5858$, S vs. PHFD $p = 0.1283$. Sucrose-inhibited: FR vs S $p = 0.0770$. Miss-inhibited: FR vs. S $p = 0.1339$, FR vs. pHFD $p = 0.0030$, S vs. pHFD $p = 0.3345$). All statistics from fat and miss trials used one-way ANOVA w/ Tukey's multiple comparisons, and sucrose trials use unpaired t-tests. **F.** Average area under the curve (AUC) Z-score responses of neurons without significant food responses (FR vs. S $p = 0.6941$, FR vs. pHFD $p = 0.3077$, S vs. pHFD $p = 0.6975$, one-way ANOVA w/ Tukey MC). **G.** Average single-neuron baseline dF/F (no food delivered) of all neurons pre- and post-HFD ($p = 0.0004$, unpaired t-test). **H**. Integral of dF/F above a threshold of session mean + standard deviation, (no food delivered) of all neurons pre- and post-HFD ($p = 0.0014$, unpaired t-test). **I.** Average neuron baseline integral dF/F over threshold per mouse, with standard error plotted. **J.** # of neurons detected per mouse pre- and post-HFD baseline imaging sessions ($p = 0.0030$, paired t-test). **K.** Body weight of mice pre- and post-HFD ($p = 0.0025$, paired t-test).

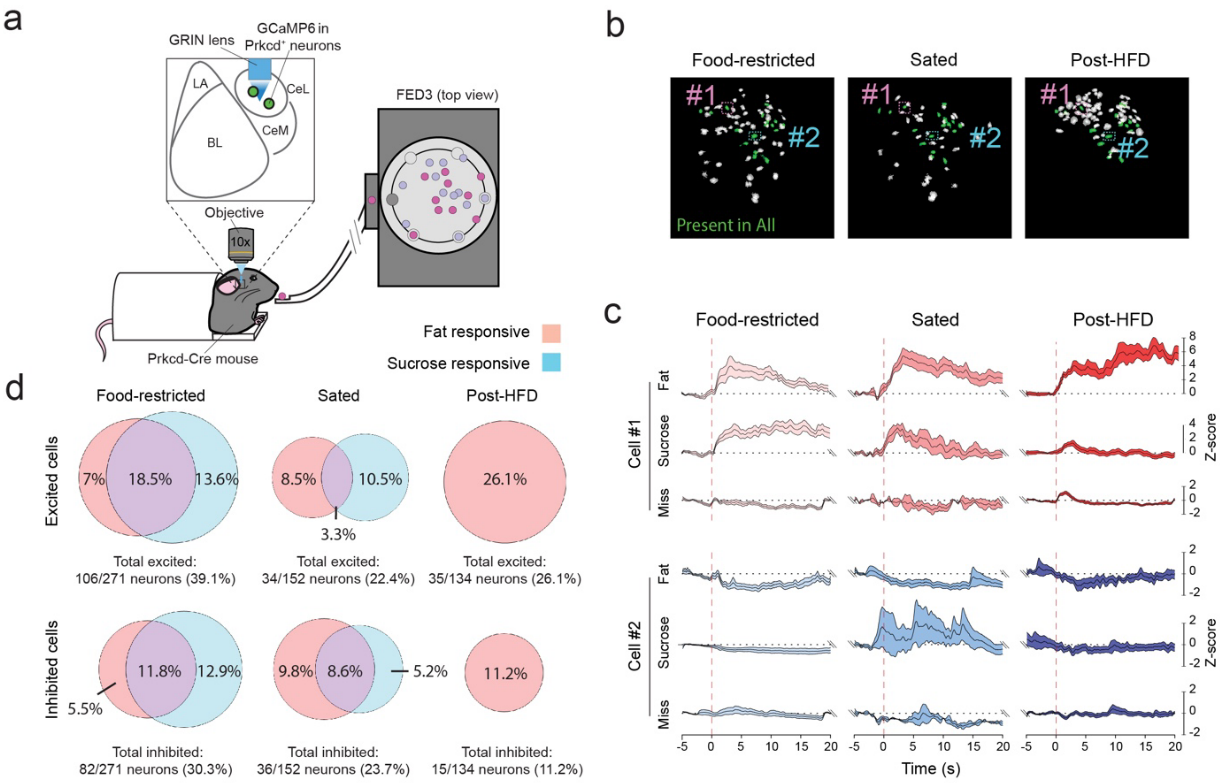

Figure 5: Extended food-imaging data
A. Experimental setup of GRIN imaging food-delivery experiments. **B.** ROIs of neurons tracked across imaging sessions, with 2 example neurons highlighted. **C.** Average activity of tracked example neurons across different metabolic states. **D.** Proportions of cells excited by fat and/or sucrose across different states (top) or inhibited (bottom), flagged using permutation tests.

2.5: Differences in preference are represented less strongly than differences in nutrient type

To determine if these neurons can distinguish between stimuli with similar composition but different caloric densities, we provided mice with the high-fat pellet and a low-fat pellet, identical except for a reduction in fat content (27% fat and 4.97 kCal/g, compared to 5% fat and 3.88 kCal/g). These pellets both differ from the sugar pellet presented previously, as the sugar pellet is made up of almost completely of sweet-tasting mono- and disaccharides (95% by calories), whereas these pellets contain a large proportion of cornstarch, a more complex carbohydrate without the sweet taste. Although these pellets have a much greater degree of overlap and similarity in their responses (Fig. 6 a-d), CeA$^{\mathrm{PKC}\delta+}$ neurons are still able to distinguish the high-fat pellet from the low-fat pellet (Fig. 6g), though with significantly lower accuracy than the high-fat pellet from the sucrose pellet. The similarity in responses suggests that preference is not strongly represented by the activity of CeA$^{\mathrm{PKC}\text{-}\delta+}$ neurons, as high-fat pellets are greatly preferred to low-fat pellets (Fig. 6j), and altering these neurons' activity does not impact preference formation (Fig.9d-e). Together, these results indicate that CeA$^{\mathrm{PKC}\text{-}\delta+}$ neuron activity encodes nutritional information about food, such as nutrient composition and calorie content, and point to a potential role for these neurons in monitoring or evaluating nutritional intake.

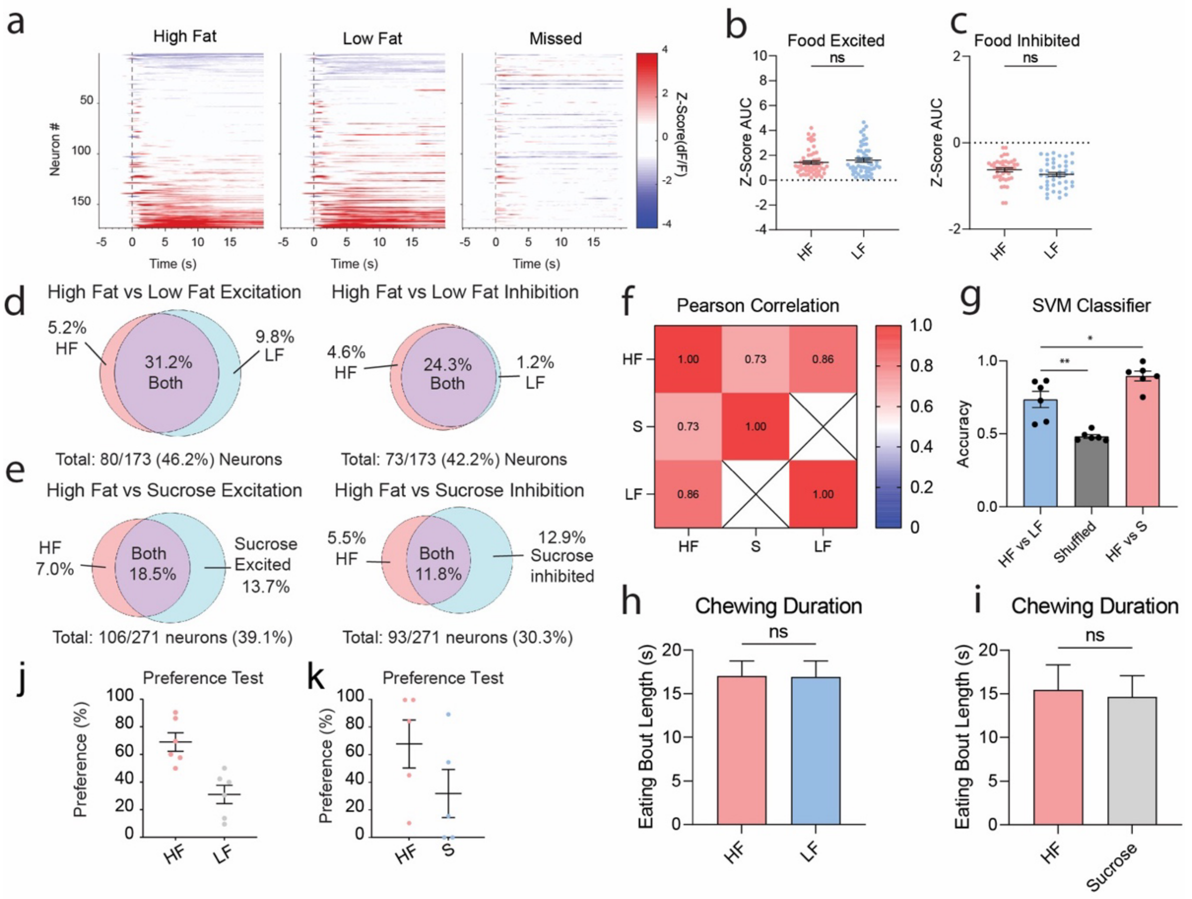

Figure 6: CeA$^{PKC\text{-}\delta+}$ neuron responses to custom high-fat and low-fat food pellets during food restriction

A. Average single neuron responses to high fat pellets (HF), low fat pellets (LF), or missed trials, with time 0 set to the moment the pellet first contacts the mouse. **B.** Excitatory responses of neurons excited by both pellets (paired t-test, p = 0.0645). **C.** Inhibitory responses of neurons inhibited by both pellets (paired t-test, p = 0.0838). **D**. Venn diagrams of cells responsive to high fat or low fat pellets (flagged using permutation test). **E**. Venn diagrams of cells responsive to high fat or sucrose pellets. **F**. Pearson correlation coefficients of average single neuron responses to each pellet type. **G**. Accuracies of SVM classifiers trained on HF vs. LF, the same dataset with shuffled labels, or HF vs. Sucrose. **H.** Chewing duration in HF vs LF imaging sessions. **I.** Chewing duration in HF vs Sucrose imaging sessions. **J.** Preference test of high fat pellet vs low fat pellet, with > 50% indicating positive preference. **K.** Preference test of high fat pellet vs sucrose pellet.

2.6: Inducing an ‘over-fed’ state increases both baseline activity and high-fat pellet response

After monitoring food responses under food-restriction (a negative energy balance) and satiety (a neutral energy balance), we exclusively fed the mice a lard-based high fat diet

(HFD, 60% fat by calories) for 2 weeks to induce a positive energy balance and promote weight gain. Indeed, all mice experienced significant weight gain after exposure to the HFD (Fig. 4k). We then recorded CeA$^{PKC\text{-}\delta+}$ neurons while feeding the high fat and sucrose pellets, as before, and in some animals we were able to track individual neurons across all 3 states (see example neurons in Fig. 5c). Mice were more likely to reject the sucrose pellets after exposure to the HFD, so the majority of the mice have full datasets only for the high fat pellet. However, we can see clear changes in the way CeA$^{PKC\text{-}\delta+}$ neurons respond to these high-fat pellets after exposure to the HFD.

Some striking differences can be seen in the single neuron average responses to the high-fat pellet (Fig 4a, d). Although the total number of fat-excited neurons post-HFD is similar to the food-restricted sessions (26.1% compared to 25.5%, Fig 5d), the post-HFD fat-excited neurons have responses that appear to be more intense and longer lasting (Fig 4a). When we quantify these responses, we see significant increases in the high-fat pellet responses in the post-HFD sessions compared to the food-restricted and sated sessions (Fig. 4d, left), while we see no differences in the responses of fat-inhibited neurons across sessions, nor in fat-unresponsive neurons (Fig 4e-f). There were also significant differences in missed-excited and in missed-inhibited responses in post-HFD sessions (Fig.4d-e, right), suggesting that CeA$^{PKC\text{-}\delta+}$ neuron signal differs both during food consumption and during food anticipation after exposure to a high fat diet.

In addition to food responses, we also investigated whether there were any changes in baseline activity during recording sessions with no food presented, recording both pre- and post-HFD (Fig. 4g-j). We found clear increases in average dF/F of individual neurons after exposure to HFD (Fig. 4g). As we are aware that dF/F may vary between recording sessions because of factors unrelated to true activity (such as differences in field of view or in illumination angle), we also calculated the integral of the dF/F above a threshold individually set for each neuron in each separate recording session (see methods). This also revealed a clear increase in baseline activity that was seen consistently in every mouse (Fig. 4h-i). Additionally, the total number of neurons we were able to extract from the baseline recording sessions increased after HFD exposure (Fig. 4k), another indication that activity increased, over all.

2.7: Synaptic input and excitability of CeA$^{PKC\text{-}\delta+}$ neurons in mice after HFD

To confirm the results of our imaging experiments and get more resolution into the synaptic changes of CeA$^{PKC\text{-}\delta+}$ neurons after exposure to HFD, we bilaterally injected AAV-fDIO-mCherry into the CeA of PKC-δ-FlpO mice and then performed whole-cell patch-clamp recordings from mCherry^{+} neurons in CeA slices of mice fed with normal chow or with HFD (Fig. 1a-b). Remarkably, feeding with HFD increased the amplitude of miniature excitatory synaptic currents (mEPSCs) recorded from CeA$^{PKC\text{-}\delta+}$ neurons (Fig. 7c-e). In contrast, feeding with HFD did not change the amplitude or frequency of miniature inhibitory synaptic currents (mIPSCs) recorded from CeA$^{PKC\text{-}\delta+}$ neurons (Fig. 7f-h). These results suggest that exposure to a high fat diet and the resulting weight gain strengthens the excitatory, but not inhibitory, synapses onto CeA$^{PKC\text{-}\delta+}$ neurons.

We further investigated whether increased excitatory input could induce hyperexcitability of CeA$^{PKC\text{-}\delta+}$ neurons by recording CeA$^{PKC\text{-}\delta+}$ neurons in slices from control or HFD-fed mice. We found an increase in the frequency of spikes in CeA$^{PKC\text{-}\delta+}$ of mice fed with HFD compared to control mice (Fig. 7i-j). To determine the effects on neuronal activity in more detail, we calculated the rheobase currents (the minimal current required to elicit an action potential) and resting membrane potentials (RMPs) of these neurons. The rheobases of CeA$^{PKC\text{-}\delta+}$ neurons in HFD-fed mice were significantly reduced, and the RMPs were enhanced, suggesting a depolarization effect (Fig. 7k-m). These findings indicate that the intrinsic activity of CeA$^{PKC\text{-}\delta+}$ neurons is enhanced after exposure to HFD, validating and complementing the *in vivo* activity increases we observed through imaging.

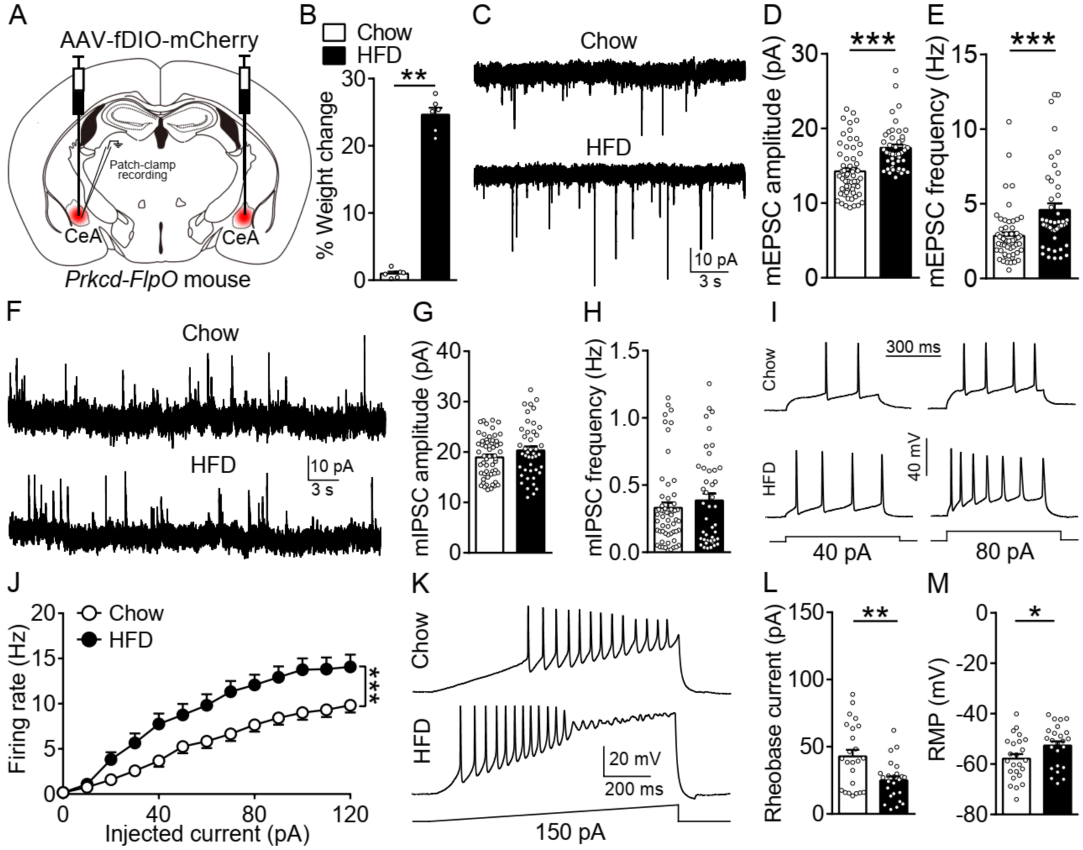

Figure 7. Increased excitatory input to CeAPKC-δ+ neurons in mice after 4-6 weeks of HFD.
A. A schematic diagram showing the sites of patch-clamp recording of CeA$^{PKC\text{-}\delta+}$ neurons. **B.** Percentages of weight change after a 4-week feeding with normal chow or high fat diet; Mann-Whitney test. **C.** Representative mEPSC traces recorded from CeA$^{PKC\text{-}\delta+}$ neurons in mice fed with normal chow (top) or HFD (bottom). **D.** Quantification of the amplitude of mEPSCs recorded from mice fed with normal chow (n = 57 neurons in 6 mice) or HFD (n = 44 neurons in 6 mice); Mann-Whitney test. **E**. Quantification of the frequency of mEPSCs recorded from mice fed with normal chow (n = 57 neurons in 6 mice) or HFD (n = 44 neurons in 6 mice); Mann-Whitney test. **F**. Representative mIPSC traces recorded from CeA$^{PKC\text{-}\delta+}$ neurons in mice fed with normal chow (top) or HFD (bottom). **G**. Quantification of the amplitude of mIPSCs recorded from mice fed with normal chow (n = 57 neurons in 6 mice) or HFD (n = 44 neurons in 6 mice); Mann-Whitney test. **H**. Quantification of the frequency of mIPSCs recorded from mice fed with normal chow (n = 57 neurons in 6 mice) or HFD (n = 44 neurons in 6 mice); Mann-Whitney test. **I-J**. Sample traces and statistical data

Figure 7 (Continued): for action potential firing recorded from CeA$^{PKC\text{-}\delta+}$ neurons in mice fed with normal chow (n = 24 neurons in 6 mice) or HFD (n = 24 neurons in 6 mice); two-way ANOVA. **K**. Example voltage responses to ramp current injections in CeA$^{PKC\text{-}\delta+}$ neurons in mice fed with normal chow (n = 24 neurons in 6 mice) or HFD (n = 24 neurons in 6 mice). **L**. Quantification of the rheobase current for CeA$^{PKC\text{-}\delta+}$ neurons in mice fed with normal chow (n = 24 neurons in 6 mice) or HFD (n = 24 neurons in 6 mice); Mann-Whitney test. **M**. Quantification of the resting membrane potential (RMP) of CeA$^{PKC\text{-}\delta+}$ neurons in mice fed with normal chow (n = 24 neurons in 6 mice) or HFD (n = 24 neurons in 6 mice); Mann-Whitney test. All error bars represent SEMs. *p < 0.05, **p < 0.01, ***p < 0.001. **Data in this figure was collected by Mingzhe Liu.**

2.8: CeA$^{PKC\text{-}\delta+}$ neurons bidirectionally modulate weight gain on a high fat diet

Given that CeA$^{PKC\text{-}\delta+}$ neurons can encode some nutritional information and that consuming HFD increases both baseline activity and acute feeding responses, we reasoned that these neurons may participate in regulating energy balance or metabolism. To test this hypothesis, we sought to selectively manipulate CeA$^{PKC\text{-}\delta+}$ neurons while using HFD to induce weight gain and metabolic changes. To specifically inhibit the activity of these neurons, we injected the CeA of PKC-δ-Cre mice bilaterally with an AAV expressing tetanus toxin light chain (TeLC, which blocks neurotransmitter release), or GFP (as a control) in a Cre-dependent manner (Fig. 8a). We then monitored the weight of the mice for 4 weeks, then placed them on a 6-week HFD (see Fig. 9b-c for a timeline diagram and histology). Remarkably, we observed starkly lower weight-gain in the TeLC mice than in their littermate GFP controls after the introduction of HFD (Fig 8b). At the endpoint of the 6-week HFD, we dissected and weighed the inguinal white adipose tissue (iWAT), the epididymal white adipose tissue (eWAT), and the brown adipose tissue (BAT). In each case, the TeLC mice had dramatically smaller fat deposits (Fig. 8c).

To investigate the possible causes of these differences, a separate cohort of TeLC mice and controls were put into metabolic cages (CLAMS), where we monitored their food intake, movement, and other metabolic parameters. After a week of habituation in the metabolic cages, the mice were fed first with their regular grain-based food (chow) for 3 days, and then with HFD for 2 weeks (Fig. 8d-i, 9b, figures use data from first 3 days of HFD). The TeLC mice were protected from weight gain on the HFD, with many of them instead experiencing weight loss in the first 3 days of HFD (Fig 8d). Interestingly, this occurred despite the fact that the TeLC mice consumed more HFD (Fig. 8e), and this increase in feeding is consistent with the results of other studies[21].

There was no change in water consumed or movement in the TeLC mice (Fig. 8f-g), showing that the lessened weight gain cannot be accounted for by decreased water intake or increased physical activity. During the chow period, there was no difference between the two groups in respiratory exchange ratio (RER), a rough measure of whether animals utilize more carbohydrates or more fat as an energy source[105]. Both groups had high values for RER during their time on chow, as expected for a high carbohydrate diet (Fig 8h). However, when the chow was replaced with HFD, the TeLC group's RER decreased significantly more during the light cycle than the GFP group's RER (Fig 8i), suggesting that the TeLC mice are utilizing more fat than expected during their inactive cycle. Over all, these results indicate that silencing CeA$^{PKC\text{-}\delta+}$ neurons prevents HFD-induced weight gain despite increased energy intake, potentially by increasing fat utilization and preventing fat storage in adipose tissue.

Next, to test whether the opposite manipulation (enhancing CeA$^{PKC\text{-}\delta+}$ neuron activity) would have an opposing effect, we used an AAV to specifically express a bacterial sodium channel (NaCh)[106] in these neurons (Fig 8, j). This channel has been shown to increase neuronal activity by lowering firing thresholds, increasing excitability, and extending action potentials[107–110]. We performed the same HFD experiments with these mice and their paired controls as discussed previously. Interestingly, the NaCh mice gained more weight than their controls during the 6-week HFD (Fig 8k), with a significant increase in iWAT mass (Fig 8l). Furthermore, the data acquired with metabolic cages revealed that the increased weight gain in the NaCh mice on HFD (Fig. 8m) was associated with an increased RER during the light cycle on HFD (Fig 8r), but with no change in food intake, water consumption, or physical activity (Fig 8n-p). These results suggest that increased $\mathrm{CeA}^{\mathrm{PKC}\text{-}\delta+}$ neuron activity may lower the utilization of fat and promote fat storage when an animal is on HFD, thereby promoting weight gain.

Altogether, our results indicate that $\mathrm{CeA}^{\mathrm{PKC}\text{-}\delta+}$ neurons bidirectionally control weight-gain and fat utilization when challenged with a HFD, and the effects are likely mediated through metabolic changes rather than changes in feeding behavior or physical activity. To further explore this possibility, we collected tissue from all groups of mice after 2 weeks of HFD (iWAT, eWAT, BAT, liver, intestine, and plasma), and submitted these samples for RNA sequencing to examine transcriptional changes and for mass spectrometry to examine differences in lipid and acylcarnitine composition. Though the analysis of this data is still underway, preliminary examinations reveal striking differences in both the TeLC mice and the NaCh mice.

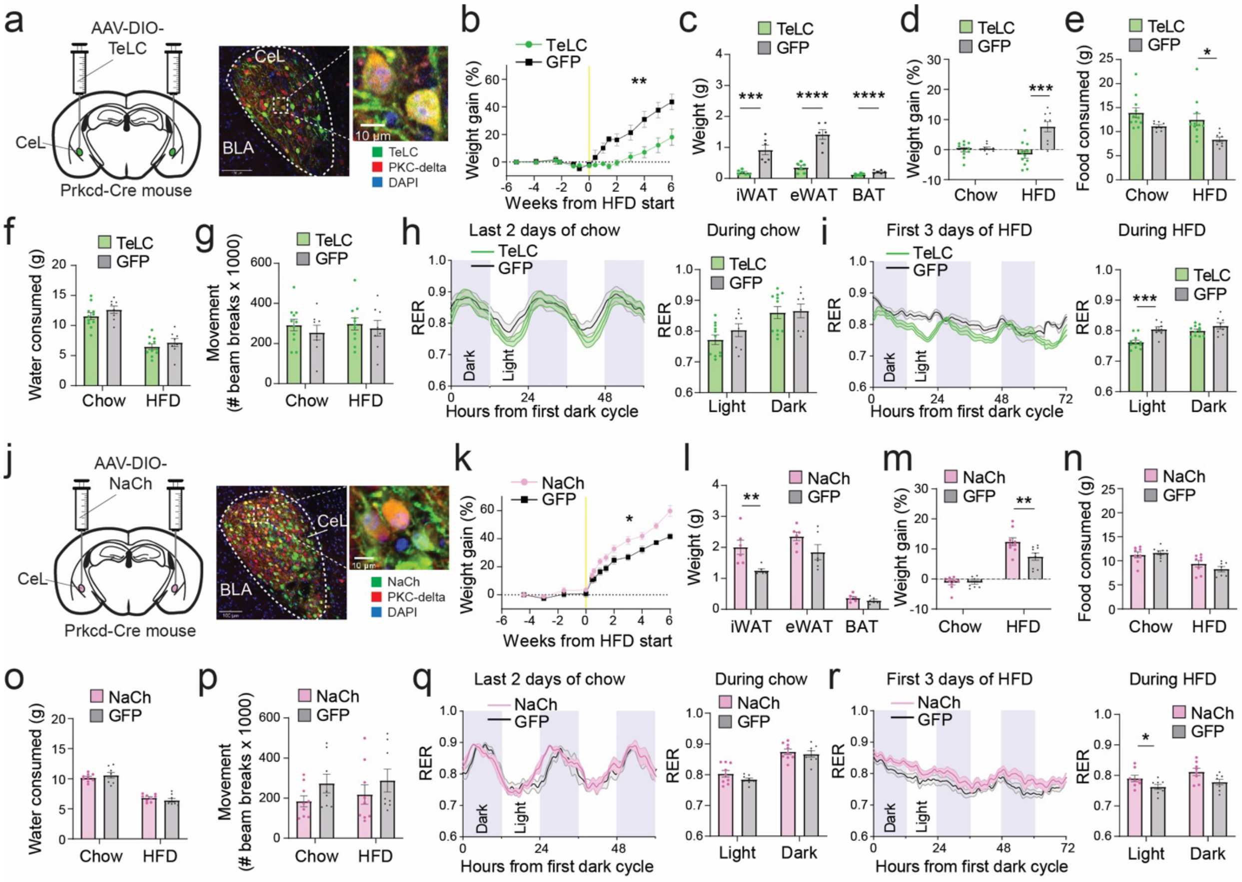

Figure 8: PKC-δ+ neurons bidirectionally modulate weight-gain and metabolism on a high fat diet
 A. Injection diagram and example histology from the CeL of a TeLC mouse, showing antibody staining for TeLC (green), PKC-δ+ (red), and DAPI (blue). **B.** TeLC weight-gain during 6 weeks of HFD (Mixed-effects: P=0.0067) **C.** Weights of TeLC adipose tissue after 6 weeks on HFD (2-Way ANOVA: P<0.0001. Sidak's test: P<0.0001, P<0.0001, P<0.0001) **D.** TeLC weight change in metabolic cages (MC): 2-Way ANOVA P=0.0003, Sidak's test: P=0.9563, P<0.0001 **E.** TeLC food consumed in MC. 2-Way ANOVA: P=0.007, Sidak's test: P=0.1046, P=0.0108 **F.** TeLC water consumed in MC (2-Way ANOVA P = 0.253 **G.** TeLC movement in MC (2-Way ANOVA P=0.537) **H.** Line graph of RER from TeLC mice in MC on chow, aligned to first dark cycle (left) and averaged by light cycle (right, 2-way ANOVA: P=0.4918, Sidak's test: P=0.4292, P=0.9752) **I.** Line graph of TeLC RER on HFD from MC (left), and averaged by light cycle (right, 2-way ANOVA: P = 0.009, Sidak's test: P=0.0005, P=0.2641) **J.** Injection diagram and example histology from the CeL of a NaCh mouse, showing NaCh (green), PKC-δ+ (red), and DAPI (blue). **K.** Average NaCh weight gain on a 6 week HFD (2-Way ANOVA: P=0.0166) **L.** NaCh average adipose tissue after 6 weeks of HFD (2-Way ANOVA: P=0.0206. Sidak's test: P=0.0236, P=0.0751, P=0.9786) **M.** NaCh weight change in MC (2-Way ANOVA: P=0.0148, Sidak's test: P= 0.9990, P= 0.0022) **N.** NaCh food consumed in MC (2-Way ANOVA: P=0.668) **O.** NaCh water consumed in MC (2-Way ANOVA: P=0.999) **P.** NaCh movement in MC (2-Way ANOVA: P=0.226) **Q.** Line graph of RER from NaCh mice in MC on chow, aligned to first dark cycle (left) averaged by light cycle (right, 2-way ANOVA: P = 0.283) **R.** Line graph of NaCh RER on HFD from MC (left), and averaged by light cycle (right, 2-Way ANOVA: P = 0.041, Sidak's test: P=0.0467,

Figure 8 (Continued): P=0.1194). This experiment was performed in collaboration with Alessandro Furlan, who assisted with experiment design and aided with some animal preparation, and with Radhashree Sharma, who assisted with dissections and takedowns. Thanks also to Jill Haber and Rachel Rubino, for managing the metabolic cage core facility.

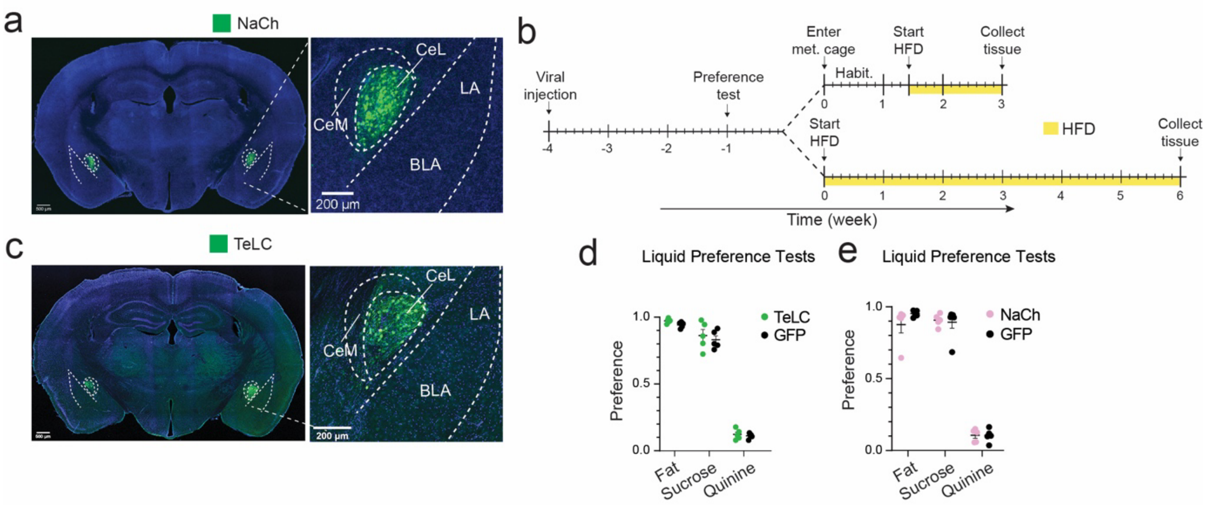

Figure 9: Extended TeLC and NaCh data
A. Example histology of a PKC-δ+-cre mouse with cre-dependent sodium channel virus delivered bilaterally to the CeA. **B**. Timeline of metabolic cage and 6 week HFD experiments, with HFD periods marked in yellow. All average metabolic cage (MC) data is from the first 60 hours of chow after habituation and the first 60 hours of HFD. **C.** Example histology from a PKC-δ+-cre mouse with cre-dependent tetanus toxin light chain (TeLC) virus delivered bilaterally to the CeA. **D.** Preference tests for TeLC vs. GFP control mice given fat, sucrose, or quinine liquid solutions (presented consecutively in a 2 bottle system with water as the alternate choice). **E.** Preference tests for NaCh vs. GFP control mice.

2.9: CeA$^{PKC\text{-}\delta+}$ neuron manipulation induces changes in adipose tissue

Next, we sought a more detailed look into how these CeA$^{PKC\text{-}\delta+}$ neuron manipulations affect fat metabolism in key metabolic pathways. We performed bulk RNA-seq on iWAT, BAT, and liver collected from either TeLC mice (with silenced activity) or NaCh mice (with increased activity) and their littermate GFP controls after 2 weeks of HFD. However, as full analysis of the RNAseq data is still underway, more detailed information into relevant metabolic pathways is not available at the time of this thesis submission, and any conclusions in this section are still speculative.

Though the RNAseq analysis is still underway, preliminary examination reveals striking results in the iWAT of TeLC mice when compared to their controls. Many genes important for adipogenesis, including *PPARg*, *Agpat2*, and *Pdgfrb* were strongly downregulated in TeLC mice. Interestingly, *Lep*, the gene encoding leptin, was amongst the most strongly downregulated genes in TeLC mice. This downregulation of leptin, an indicator of satiety and inhibitor of feeding, may potentially explain the increase in feeding seen in TeLC mice. Additionally, *DGAT1* and *DGAT2*, both involved in synthesizing TGs, were also downregulated, suggesting that the TeLC may indeed be storing less fat than their controls, though these results have yet to be validated. Preliminary mass spectrometry also revealed differences in iWAT fatty acid composition (Fig. 10). Generally, TeLC mice had a larger amount of fatty acids in iWAT when compared to their controls, and the opposite was seen in the NaCh. Though these experiments are still in the process of being completed and analyzed, the initial indication is that CeA manipulations indeed influence both adipose tissue composition and gene expression. There is much more information left to extract from these experiments, and more analysis and validation is needed to fully explore the effect of these CeA manipulations on metabolism.

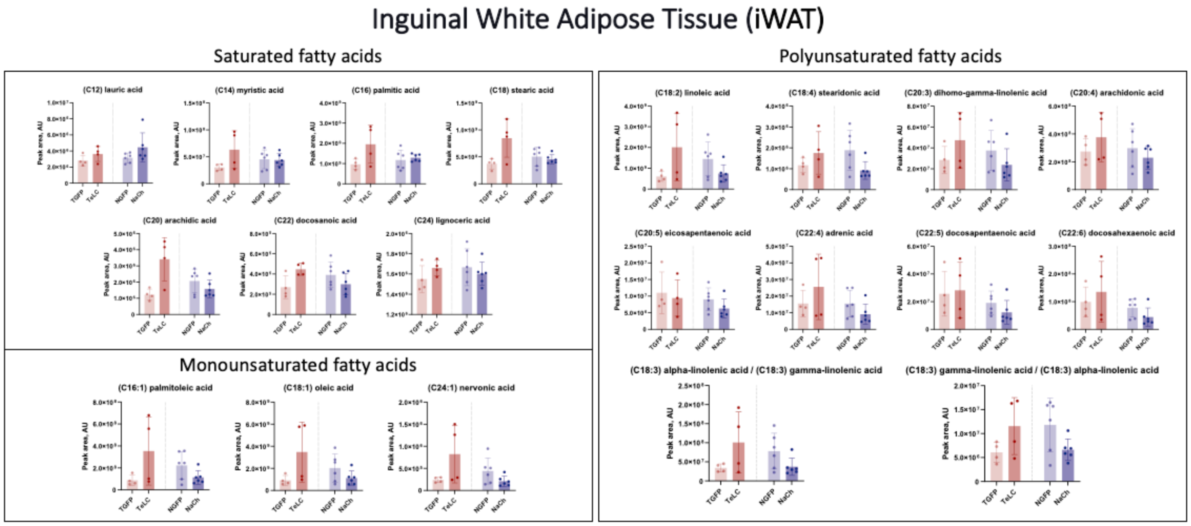

Figure 10: Preliminary mass spectrometry results reveal differences in iWAT FAs
Amounts of selected types of saturated, polyunsaturated, and monounsaturated fatty acids from the iWAT of TeLC vs. control (TGFP) and NaCh vs. control (NGFP) mice fed 2 weeks of HFD. Preliminary work from Ece Kilic and Paolo Cifani (CSHL mass spectrometry core) in collaboration with Justin Cross and Sara Violante (MSKCC). Fat pad dissections were done with help from Radhashree Sharma. Daniëlla van de Lisdonk and Radhashree Sharma assisted with RNA extractions, though the resulting RNAseq data is still being analyzed.

2.10: Potential circuits

As CeA manipulation has clear effects on metabolism and weight gain, we next performed tracing experiments to elucidate potential pathways through which CeA$^{PKC\text{-}\delta+}$ neurons could be exerting their effects. Anterograde tracing of CeA$^{PKC\text{-}\delta+}$ neurons (Fig. 11 a-b) revealed projections in brainstem areas (Fig. 11 d), and retrograde tracing using CTB confirmed CeA$^{PKC\text{-}\delta+}$ projections to the NTS (Fig. 11 e-h), an area already known for its role in feeding[87,111], adiposity resistance[112], and for integrating vagal information from the periphery to influence feeding, as part of the parasympathetic nervous system[113]. Though direct parasympathetic innervation of iWAT is very sparse, vagus nerve signaling is required for lipolysis of adipose tissue during fasting[114]. Brain areas involved in sympathetic and somatosensory innervation of adipose (see section 1.7) are also potential targets of interest to understand how the CeA may be exerting its effects on metabolism. For a preliminary survey of circuits that indirectly innervate white adipose tissue, we injected white adipose tissue with multi-synaptic pseudorabies virus (PRV; Fig. 11i-j). We found that most labeled cells in the central amygdala were in the CeM, though some CeA$^{\text{PKC-}\delta+}$ neurons in the CeL contained PRV as well. This suggests the possibility that CeA$^{\text{PKC-}\delta+}$ neurons may be connected to circuits that directly regulate WAT, but more experiments are needed to confirm this.

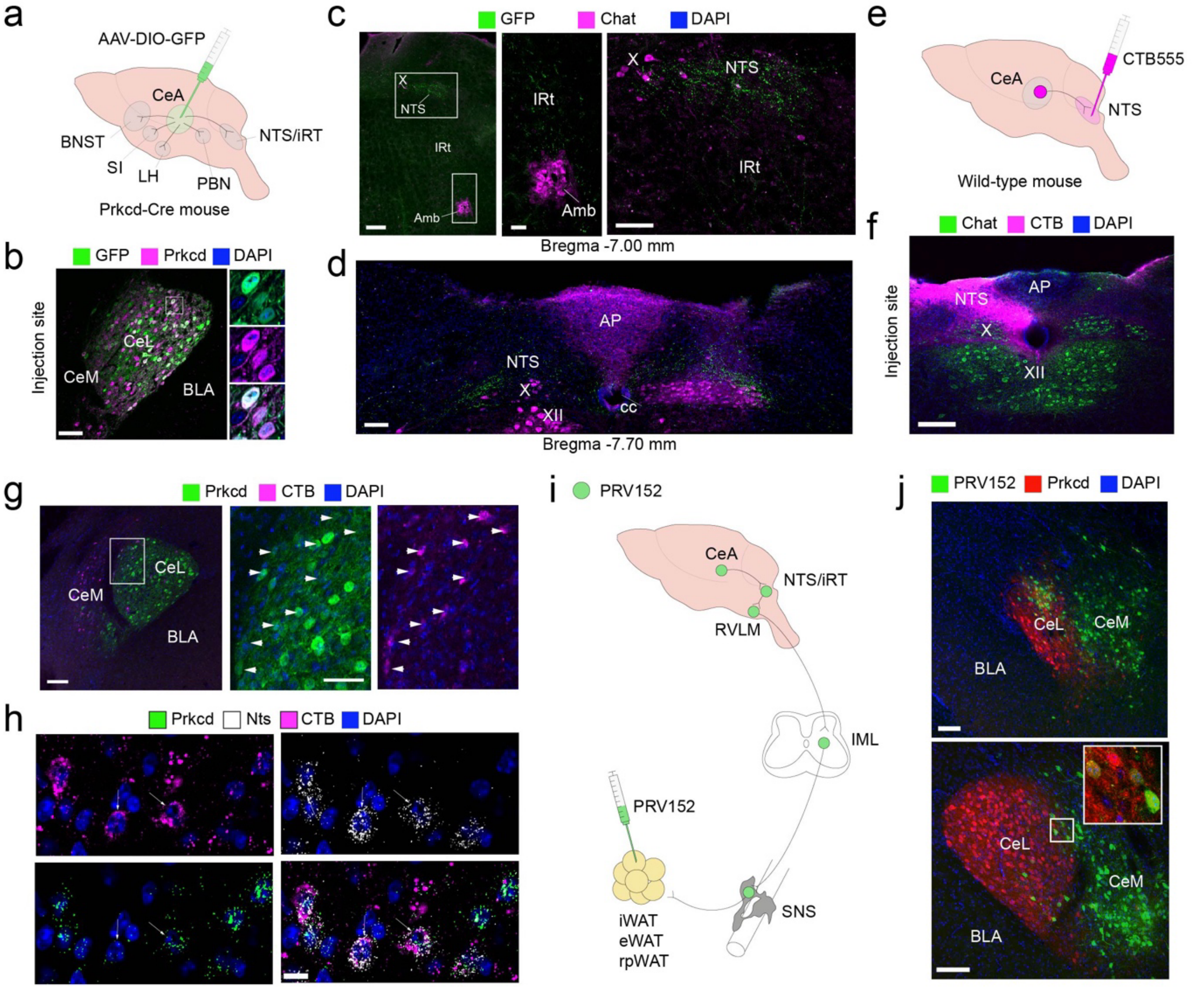

Figure 11: Tracing potential CeA circuits in fat metabolism

A. Schematic of the approach for anterograde tracing. B. Representative image of the injection site. Scale bar: 100um (n=1). C-D. CeAPKC-δ neurons innervate the DMV area. C. left: CeAPKC-δ neurons innervate the rostral NTS. Scale bar: 100 um (n=1) middle: CeAPKC-δ neurons innervate the Nucleus Ambiguus (Amb). Scale bar: 50 um (n=1), right: CeAPKC-δ neurons innervate the caudal NTS. Scale bar: 100 um (n=1). **D**. Overview of the innervation of CeAPKC-δ neurons in the brainstem. Scale bar: 200um. **E.** Schematic of the approach for monosynaptic retrograde tracing using CT-B (n=1). **F**. Representative image of the injection site (the NTS). Scale bar: 200um (n=1). **G.** Representative image of the CeA showing double positive PKC-δ+CTB555+ neurons (arrowheads). Scale bar: 100 um (left), 50 um (center and right). (n=1). **H**. Representative image of the CeA showing double positive PKC-δ+Nts+CTB555+ neurons (arrows). Scale bar: 10 um (n=1). **I**. Schematic of the approach for tracing from white adipose tissue (WAT) deposits (n=1). **J**. Representative image of the rostral (top panel) and caudal (bottom panel) CeA showing double positive PKC-δ+PRV+ neurons. Scale bar: 100 um. (n=1). **Data in this figure was collected by Alessandro Furlan (a-h) and Radhashree Sharma (i-j).**

Chapter 3: Conclusions and Perspectives

We examined the responses of $\mathrm{CeA}^{\mathrm{PKC}\text{-}\delta+}$ neurons to various foods across different metabolic states and observed that $\mathrm{CeA}^{\mathrm{PKC}\text{-}\delta+}$ neuron activity reflects both acute food responses and also chronic energy imbalances. Surprisingly, for a population known to respond to pain[24,45], activity seems to encode the stimulus's nutritional or physical properties rather than valence or preference. Aversive quinine responses are represented more similarly to water than to air puff, suggesting that these neurons are sensitive to sensory modality but not necessarily to valence. High-fat pellets and sucrose pellets, both of which are high value foods containing different nutritional components, have less overlap in responses when compared to high-fat and low-fat pellets, stimuli which have large differences in preference but relatively similar nutrient composition (the main difference being proportion of fat). Consistent with this, manipulating $\mathrm{CeA}^{\mathrm{PKC}\text{-}\delta+}$ neuron activity does not impact preference formation (Fig. 9d-e), suggesting that $\mathrm{CeA}^{\mathrm{PKC}\text{-}\delta+}$ neuron responses to consummatory stimuli may be more linked to nutrition than to preference.

Using the high-fat and the sucrose pellets, we were able to compare $\mathrm{CeA}^{\mathrm{PKC}\text{-}\delta+}$ neuron food responses across food-restriction, satiety, and post-HFD conditions. From these experiments, we see that $\mathrm{CeA}^{\mathrm{PKC}\text{-}\delta+}$ neurons respond robustly to food and carry enough information to encode the identities of the pellets, whether the mice are food-restricted or sated, suggesting that these neurons identify and potentially evaluate foods for nutritional value. A potential avenue for how the $\mathrm{CeA}^{\mathrm{PKC}\text{-}\delta+}$ neurons could be able to do this might be from the robust insula projections to the CeL[51]. As the insula is known for processing taste, this pathway may play some role in the way the CeA is able to evaluate food and warrants further exploration. Additionally, we report significant proportions of $\mathrm{CeA}^{\mathrm{PKC}\text{-}\delta+}$ neurons with inhibitory responses to food (almost matching the number of neurons with excitatory responses; Fig. 5d). This type of food response has not been reported before from $\mathrm{CeA}^{\mathrm{PKC}\text{-}\delta+}$ neurons, and these diverse responses may be an indication of mixed cell-type populations that would benefit from closer study.

Additionally, we found that a 2-3 week HFD feeding regimen changed how $\mathrm{CeA}^{\mathrm{PKC}\delta+}$ neurons respond to the high-fat pellets. It is well-known that neurons in the CeA, including $\mathrm{CeA}^{\mathrm{PKC}\text{-}\delta+}$ neurons, undergo experience-dependent functional changes during learning[24,29], and stimulus responses in CeA neurons can be amplified through repeated experience. It is possible something similar is happening here, as prolonged exposure to a high fat diet significantly increases responses to the high-fat pellet during feeding. Remarkably, there is also an increase in baseline activity that we observed both in imaging experiments and through slice physiology, demonstrating that HFD alters the activity of $\mathrm{CeA}^{\mathrm{PKC}\text{-}\delta+}$ neurons even in the absence of food. This suggests that in addition to altering the way they acutely respond to food, $\mathrm{CeA}^{\mathrm{PKC}\text{-}\delta+}$ neurons also increase their overall activity to reflect the positive energy balance and weight gain induced by dietary changes.

After observing the changes in neuronal activity induced by HFD, we used genetic tools to artificially manipulate $\mathrm{CeA}^{\mathrm{PKC}\text{-}\delta+}$ neuron activity to either block activity (with TeLC) or enhance it (with NaCh), then monitored the effects on metabolism before and after switching the mice to a HFD. Surprisingly, $\mathrm{CeA}^{\mathrm{PKC}\text{-}\delta+}$ neurons modulate weight gain on HFD in a bidirectional manner. Inhibition is protective against weight gain and increased adiposity, despite causing mice to increase feeding. This increased feeding is consistent with the work from other groups[21,50], though to our knowledge, this is the first work that has manipulated PKC-δ+ neurons while challenging animals' metabolisms with HFD. In contrast to the effects of the TeLC inhibition, increasing $\mathrm{CeA}^{\mathrm{PKC}\text{-}\delta+}$ neuron activity by expressing NaCh increased the weight gain caused by HFD without changing feeding habits. Nether manipulation caused any changes in water consumption or movement.

This is the first manipulation to show that over-activating CeA$^{\text{PKC-}\delta+}$ neurons has an impact on fat storage, unrelated to level of food consumption. Other groups have activated CeA$^{\text{PKC-}\delta+}$ neurons using ChR2[21], and as a result they report reductions in feeding. However, work from our group has demonstrated that this synchronous stimulation of CeA$^{\text{PKC-}\delta+}$ neurons with ChR2 can be aversive[24], which would confound any reported effects on feeding. Using NaCh to over-activate CeA$^{\text{PKC-}\delta+}$ neurons is a more naturalistic long-term manipulation, as it likely preserves some of the natural timing of the local network and does not induce artificial synchronization of the entire population. For these reasons, we believe we were able to observe a previously unreported consequence of boosting CeA$^{\text{PKC-}\delta+}$ neuron activity.

Together, this data demonstrates that weight gain triggered by changes in diet coincides with and is driven by increased CeA$^{\text{PKC-}\delta+}$ neuron activity, both in response to palatable food and in the absence of any stimuli. Increased CeA$^{\text{PKC-}\delta+}$ neuron activity does not inhibit feeding. Rather, it seems to signal a state of positive energy balance, potentially indicating that more calories have been consumed than strictly needed. This increased activity may then cue these extra calories to be stored as fat, as seems to be the case for the NaCh animals. Similarly, inhibiting CeA$^{\text{PKC-}\delta+}$ neuron activity with TeLC does indeed increase feeding, as previously reported by others, but the increase in food intake is starkly contrasted by the resistance to weight gain. Although we are still investigating which metabolic pathways are the effectors of these differences, this suggests that CeA$^{\text{PKC-}\delta+}$ neuron activity is needed for excess calories to be properly stored in adipose tissue.

Silencing these neurons may prevent fat storage and cause animals to increase their utilization of fat, potentially mimicking a metabolic state similar to starvation.

These results directly oppose the current understanding of the role of CeA$^{\text{PKC-}\delta+}$ neurons and support an important role for the CeA in metabolism. Although some experiments are still ongoing, it is clear that CeA manipulation has far-reaching effects on metabolism, especially on fat processing. This project demonstrates that exposure to a high fat diet and significant weight gain fundamentally alters the CeA$^{\text{PKC-}\delta+}$ neurons' activity and responses to food. Here, we demonstrate a bidirectional causative link between CeA$^{\text{PKC-}\delta+}$ activity and weight gain on a HFD.

Chapter 4: Experimental Procedures

4.1: Mice

Male and female mice (2-8 months old) were used for all experiments, with all experimental and control groups consisting of paired mice from the same litter. Mice were housed under a 12-h light/dark cycle (7 a.m. to 7 p.m. light) in groups of 2-5 animals, with the exception that mice with GRIN lens implantation were housed individually. Food and water were available *ad libitum* before the start of experiments. All experiments were performed during the light cycle. Littermates were randomly assigned to different groups prior to experiments. All mice were bred onto a C57BL/6J background. All experimental procedures were approved by the Institutional Animal Care and Use Committee of Cold Spring Harbor Laboratory and performed in accordance to the US National Institutes of Health guidelines.

Transgenic mice used include *PKC-δ+*^{Cre} (strain number: #, stock code: #) and *PKC-δ+*^{Flp} (strain number: #, stock code: #).

4.2: Stereotaxic surgery

Standard surgical procedures were used for stereotaxic injection and implantation, as previously described[115]. All surgery was performed under aseptic conditions and body temperature was maintained with a heating pad. Mice were anaesthetized with isoflurane (1-2%, as needed) and given preemptive anti-inflammatory and pain medicine prior to surgery (5 mg/kg Metacam) then positioned in a stereotaxic frame. The frame was linked to a digital mouse brain atlas to guide the targeting of different brain structures (Angle Two Stereotaxic System; Leica Biosystems Division of Leica, Buffalo Grove, IL 60089, USA). The following stereotaxic coordinates were used for CeA: -1.18 mm posterior from bregma, 2.9 mm lateral from the midline, and 4.6 mm vertical from skull surface.

Viral injections

For virus injection, we made a small cranial window (1–2 mm wide) and delivered ~0.3 µl of virus into the brain through a glass micropipette (tip diameter, ~5 µm) by pressure application (5–20 psi, 5–20 ms pulses at 0.8 Hz) controlled by a Picrospritzer III (General ValveParker， Hollis, NH, USA) and a pulse generator (Agilent).

The pAAV-Syn-Felx-GCaMP6m-WPRE-SV40 (AAV1) was purchased from Addgene (Watertown, MA 02472, USA). The AAV8-Ef1a-fDIO-GCaMP6f was produced by K. Deisseroth’s lab at Stanford University. All viruses were stored in aliquots at -80 °C until use.

Fiber photometry

For *in vivo* fiber photometry experiments, optical fiber implantation was performed after the viral injection in the same surgery. Optical fibers (core diameter, 200 µm; length, 5 mm; NA, 0.37; Inper Corporation, Hangzhou, China) were bilaterally implanted and placed using the injection coordinates for the CeA.

GRIN lens surgeries

For in vivo imaging with gradient-index (GRIN) lenses, we injected virus as described, then performed a second surgery one week after injection to implant the GRIN lens (diameter: 600 µm; length: 7.3 mm; Inscopix, Palo Alto, CA 94303, USA). To implant the lens, we first widened the cranial window using a drill, and then used an adaptor (Inscopix) to hold and carefully lower the GRIN lens through the window into the target area at a low speed (~100 µm/min). We then fixed the GRIN lens in place using Metabond adhesive cement (Parkell Products Inc, Edgewood, NY, USA) and dental cement (Lang Dental Manufacturing Company, Wheeling, Illinois, USA). The holder was released after the cement was completely cured. A metal head-bar (for head-restraint) was mounted onto the skull with black dental cement. (Ortho-Jet). Mice were monitored for signs of pain and given Metacam post-operatively as needed. They were given 6 weeks of recovery before starting imaging experiments.

4.3: Immunohistochemistry

Immunohistochemistry experiments were conducted following standard procedures. Briefly, mice were anesthetized with Euthasol (0.4 ml; Virbac, Fort Worth, Texas, USA) and transcardially perfused with 30 ml of PBS, followed by 30 ml of 4% paraformaldehyde (PFA) in PBS. Brains were extracted and further fixed in 4% PFA overnight followed by cryoprotection in a 30% PBS-buffered sucrose solution for 48 h at 4 °C. Coronal sections (50 µm) were cut using a freezing microtome (Leica SM 2010R, Leica).

Sections were first washed in PBS (5 min), incubated in PBST (0.3% Triton X-100 in PBS) for 30 min at room temperature (RT) and then washed with PBS (3 x 5 min). Next, sections were incubated with primary antibodies overnight at 4 °C. The next day, sections were washed with PBS (3 x 5 min) and incubated with fluorescent secondary antibodies at RT for 2 h. After washing with PBS (3 x 5 min), sections were mounted onto slides with Fluoromount-G (eBioscience, San Diego, California, USA). Images were taken using a LSM 710 laser-scanning confocal microscope (Carl Zeiss, Oberkochen, Germany). The primary antibodies used were: chicken anti-GFP (Aves Labs, catalogue number GFP1020, lot number GFP697986; dilution 1:1000), rabbit anti-PKC-δ+ (Need virus info). Appropriate fluorophore-conjugated secondary antibodies (Life Technologies) were used depending on the desired fluorescence colors.

4.4: One photon imaging experiments

All experiments used custom Matlab protocols written for Bpod (Sanworks) to deliver stimuli and/or monitor spout licks, trigger cameras, and sync stimulus delivery with one photon data. One photon video acquisition was accomplished using a PixelFly camera, and Logitech webcams were used for monitoring the mice and recording food delivery.

<u>6-spout delivery experiments:</u>

Mice were initially water-restricted for 2 days and habituated to the head-fixed imaging rig in 20 minute sessions with no stimulus delivery. They were then trained to drink water from a 6-spout delivery system and connected to a circuit to electrically measure spout licks. When mice showed consistent licking behavior, the delivery system was filled with test solutions and calibrated between each imaging session for consistent volume delivery. The 6-spout system was built using independent tubing for 6 liquid stimuli, combined with a triggerable vacuum to remove excess liquid. The stimuli delivered were: Intralipid fat emulsion (diluted to 5% fat content), 12.5% sucrose solution, water, .1% xanthan gum (Sigma Aldrich), mineral oil (Sigma Aldrich), and .5 mM quinine (Sigma Aldrich). Additionally, during recording sessions, an air puff spout was positioned in front of the eye to randomly deliver puffs of air to the mouse. All liquids and air puffs were delivered in a random order, with unrecorded water trials delivered in between each stimulus to act as a cleanser and ensure there is no contamination from previous trials, in addition to vacuuming excess liquid away between every trial.

<u>Food-delivery experiments:</u>

Food pellets were delivered using a feeding experimentation device (FED3) modified for use in head-fixed experiments. All imaging sessions included either custom ordered 20 mg high fat pellets (Bio-Serve, 27% fat by calories, 4.97 kcal/g) and high sucrose pellets (Bio-Serve, 95% sugar by calories, 3.84 kcal/g), or high-fat pellets and low-fat pellets (Bio-Serve, 5% fat by calories, 3.88 kcal/g). The pellets were delivered randomly, and cameras were used to verify the identity of the pellets and to score the precise timing of delivery. For food-restricted pellet delivery experiments, mice were head-fixed and habituated to the rig for 20 minutes, then food restricted overnight. The next day, mice were head-fixed and trained to eat all types of experimental pellets in order to habituate the mice to each type of food before recording. The food-restricted mice were tested during imaging the next day on randomly delivered high fat and high sucrose food pellets, for a total of 50 trials. This was repeated on the following day using high fat pellets and low fat pellets. For sated imaging sessions, mice were given a minimum of one week to recover from food restriction with full access to food and water before being retested on the high fat and high sucrose pellets. As these pellets were much more appetitive than the low-fat pellets, most mice freely participated in sated imaging sessions (though they completed fewer trials than under food-restriction).

Next, to measure responses after exposure to a high fat diet, mice were tested with mild food restriction (6 hours during the light cycle) and given high-fat pellets while imaging. Once this was complete, the mice were put on high fat diet (HFD; 60% fat by calories, lard based, from Bio-serv) for 2 weeks. Afterwards, the mice were tested on the high fat pellets alone, first while sated, and next, with a 6 hour food restriction during the light cycle. High fat pellets were used because after 2 weeks of high fat diet, most mice performed fewer trials while on the rig, and only one pellet type could be given with certainty that 5 or more trials would be completed. The mild 6 hour food restriction data was used to compare pre and post high fat diet imaging data in cases where mice refuse the pellets after exposure to high fat diet. Mice were weighed after all imaging sessions to monitor weight gain/loss.

GRIN Imaging Baseline Recording Experiments

To measure activity during periods without exposure to food, mice were placed on the rig with both the food pellets and the pellet delivery spout removed. After 30 minutes of habituation, 10 trials of 25 second duration were recorded in the absence of any explicit stimuli. Each trial had a 2-2.5 minute inter trial interval.

4.5: One Photon Data Analysis

All one photon imaging data was saved in a .TIF format, pre-processed to minimize motion artifacts using NoRMCorre[116], and processed using CNMF_E[117] to extract single cell information. All resulting neurons were thoroughly screened for quality, and trials were aligned to first stimulus contact, using Bpod and camera data to synchronize behavior with the signal. Z-score was calculated individually for each neuron, using the first 4 seconds of every trial as baseline for the calculation over the course of the whole session.

6-Spout Analysis

We clustered neurons based on their average response trace to each stimulus using 9-nearest neighbors clustering (optimal number of clusters was determined using a Silhouette test). We constructed a Pearson correlation matrix using the Pearson correlations of each pair of stimuli, then used the calculated correlation coefficients as a distance metric to perform hierarchical clustering of the stimuli. We performed t-distributed stochastic neighbor embedding (t-SNE) using 20 single trial responses for each stimulus (140 trials total), combining the single neuron responses from all mice (5 mice, 270 neurons). We then constructed a linear classifier using the t-SNE output and tested it using 10-fold cross validation over 100 different t-SNE constructions to obtain classifier accuracy. To visualize the most likely trials to fail in classification, we used a representative t-SNE plot, trained a linear classifier using the Matlab function, fitcdiscr, then used the function resubPredict calculate the resubstitution error and predict class labels for the dataset (with resubstitution), marking the misclassified trials with an X, as a method to evaluate classifier performance on individual trials.

Food Delivery Analysis

We constructed heatmaps of average individual neuron responses sorted by high fat pellet response. For each mouse, we used PCA to reduce dimensionality of single neuron responses to each food-pellet, then built SVM classifiers using the average single neuron responses of each trial (either high fat or high sucrose trials) as the input, using leave-one-out cross validation to predict accuracy. As a control, we shuffled the trial labels randomly and trained the classifier using the shuffled data. Equal numbers of each trial type were used for training the classifiers. Cell tracking between imaging sessions was performed using cellReg[118], and responsive neurons were flagged by performing permutation tests using single trial baseline responses vs. 10 second stimulus responses, using shuffled baseline/response data as a control, and selecting all neurons with significant ($p < .05$) stimulus responses when compared to baseline.

Baseline Analysis (No Food Delivered)

To calculated baseline activity, baseline recording sessions were processed the same way as previously described to extract single neuron activity. As Z-score is not an appropriate calculation for a session with no stimuli delivered and by its nature would mask any differences in baseline-only sessions, mean dF/F was calculated by taking the average over the entire session. I chose to calculate the integral over a threshold as a different measure of activity meant to be less vulnerable to changes in fluorescence due to alterations in illumination or field of view. This threshold was individually chosen for each neuron by adding the mean dF/F to the standard deviation of dF/F from the entire session, then the integral of the signal above this threshold was calculated.

4.6: High fat diet experiments

Metabolic cages

Mice were first injected with cre-dependent TeLC virus, cre-dependent NaCh virus, or with cre-dependent GFP virus, as described. All experimental mice (TeLC or NaCh) were prepared with paired littermate controls (GFP) on the same day. After 3 weeks, mice were singly housed and habituated to the metabolic cages (CLAMS, Columbus) for at least one week before testing, under a 12-h light/dark cycle (6 a.m. to 6 p.m. light). Mouse locomotion (infrared beam breaks in the XYZ axis), energy expenditure (EE), oxygen consumption (VO_2), carbon dioxide production (VCO_2), respiratory exchange ratio (RER), food intake, and water intake were recorded. Data was exported using the Clax software. For 72h visualizations, data was binned in 1h intervals. Heat data (re-named energy expenditure, EE) was normalized to body weight. The mice were first fed with regular chow (PicoLab Rodent Diet 20, Cat. No. #5053*; physiological value, 3.43 kcal/g) for 10 days, and then with HFD (Bioserv, Cat. No. # S3282; physiological value, 5.49 kcal/g) for 2 weeks. Food and water were available *ad libitum* during testing. Gas sensor calibration (CO_2, O_2) of the apparatus was performed before each test. Mouse bodyweight was recorded prior to and after every testing session. Afterwards, we collected blood samples, then sacrificed the mice and harvested iWAT, eWAT, BAT, jejunum, liver, and the brain to confirm injection accuracy.

6-week high fat diet

Mice were singly housed to aid in monitoring food-intake. Mice were first injected with cre-dependent TeLC virus, cre-dependent NaCh virus, or with cre-dependent GFP virus, as described. All experimental mice (TeLC or NaCh) were prepared with paired littermate controls (GFP) on the same day. Initial bodyweight was recorded at the time of injection, then monitored for 30 days while mice were fed regular chow. Blood samples were collected through tail vein bleeds (no more than 200 uL), then mice were switched to high fat diet and monitored for 6 weeks. Afterwards, we collected blood samples, then sacrificed the mice and harvested iWAT, eWAT, BAT, jejunum, liver, and the brain to confirm injection accuracy.

Insulin tolerance test (ITT) & glucose tolerance test (GTT)

Singly housed mice were transferred to a clean cage, with food removed for 6 hours (9 a.m. – 3 p.m.) before each test. All tests started at 3 pm. For ITT, mice were injected intraperitoneally (i.p.) with 0.5 U/kg body weight insulin (Humulin, Eli Lilly; NDC Code: 0002-8215) in 0.9% sterile saline. For GTT, mice were injected i.p. with 1 g/kg bodyweight glucose (Sigma G5767-25G) in 0.9% sterile saline. There was a 48-h gap between tests, during which food and water were available *ad libitum*. Blood glucose levels were measured in duplicates at 0, 15, 30, 45, 60, 90, and 120 minutes after injection using OneTouch Ultra 2 Glucometer (OneTouch).

4.7: Electrophysiological Experiments

Surgery for viral injection into the brain

The synaptic inputs and excitability of CeA$^{PKC\text{-}\delta+}$ neurons in obese mice were examined by injecting AAV-Ef1α-fDIO-mCherry (AAV2/1, titer: 4 × 10^{12} v.g./mL, addgene) bilaterally into the CeA of *PKC-δ-FlpO* mice (8 weeks old). These mice were fed with normal chow or HFD subjected to slice electrophysiology experiments 4-6 weeks later.

Electrophysiological slice recording

Slice electrophysiology was performed as described previously. Adult (8- to 16-week-old) mice were deeply anesthetized by an overdose of isoflurane. Their brains were extracted, and coronal brain slices (220-300 µm) were generated at a slicing speed of 0.12 mm/s in ice-cold cutting solution containing 110 mM choline chloride, 25 mM $NaHCO_3$, 1.25 mM NaH_2PO_4, 2.5 mM KCl, 0.5 mM $CaCl_2$, 7.0 mM $MgCl_2$, 25.0 mM glucose, 11.6 mM ascorbic acid and 3.1 mM pyruvic acid, gassed with 95% O_2 and 5% CO_2 (300-310 mOsm) using a vibrating blade microtome (HM650, Thermo Fisher Scientific). The slices were transferred to the holding chamber and incubated in 34 °C ACSF containing: 118 mM NaCl, 2.5 mM KCl, 26.2 mM $NaHCO_3$, 1 mM NaH_2PO_4, 20 mM glucose, 2 mM $MgCl_2$ and 2 mM $CaCl_2$, which was oxygenated with 95% O_2/5% CO_2 (300–310 mM). Forty-five minutes after recovery, the slices were transferred to a recording chamber and perfused with oxygenated ACSF at 3 mL/min at room temperature or 30–32 °C. Whole-cell patch-clamp recordings were performed using glass pipettes with a resistance of 3–5 MΩ. For action potential recording experiments, $CeA^{PKC\text{-}\delta+}$ neurons were recorded in current-clamp mode using potassium-based internal solution with application of CNQX (10 µM), D-AP5 (50 µM) and picrotoxin (PTX; 50 µM) to block excitatory and inhibitory synaptic inputs. The locations of recorded $CeA^{PKC\text{-}\delta+}$ neurons were visualized with an air objective (4×; NA 0.13). mEPSCs were recorded at a holding voltage of -70 mV, and mIPSCs were recorded at a voltage of 0 mV with application of tetrodotoxin (TTX, 1 µM).

Statistical analysis

Current clamp recordings were carried out using a computer-controlled amplifier

(MultiClamp 700B; Molecular Devices). During recordings, traces were low-pass filtered at 4 kHz and digitized at 20 kHz (Digidata 1440A; Molecular Devices). The data were acquired with Axon Clampex 10.2 software. The amplitude and latency of the mEPSCs and mIPSCs were measured from the software Minianalysis. Statistical analysis was performed using Igor Pro (WaveMetrics) and Prism (GraphPad Software). All statistical analyses were two-tailed comparisons. The data were analyzed using the Mann-Whitney test and two-way ANOVA. All data are expressed as the mean ± SEM.

Acknowledgements

Here I will thank the people (and animals) that made it possible for me to survive and muddle through my doctoral experience. First, I'd like to thank my friends and family, whose support was much needed through some very trying times. Thank you to my manor family, for being a constant source of support and friendship throughout an otherwise incredibly isolating pandemic. Thank you to my partner, for keeping me supplied with tea and for being an excellent captive audience for practice talks. Thank you to my family for being cool with me running off to different states every few years, and for telling me they're proud of me for even my smallest accomplishments.

A lot of the work I presented here was only possible because of the mentorship and inspiration I received from my colleagues and friends in the Li Lab (you know who you are). I was lucky to work in an environment that allowed me to follow my interests and explore new paths, and I'm grateful for the support and guidance (and chocolate) that kicked off a completely new and unexpected research direction these past few years. Big thanks to Bo for his enthusiastic support of my research, and for giving me the freedom to pursue a much, much cooler thesis project than I had originally planned.

I also want to thank my thesis committee for their support and feedback, and my collaborators in the Li Lab, Beyaz Lab, the CSHL metabolic cage core facility, the CSHL mass spectrometry core, Memorial Sloan Kettering Cancer Center (MSKCC), and the New York Genome Center (NYGC). Thank you very much for your help with experiments and your contributions to the data presented here. I didn't want to accidentally leave anyone out here, so look for your names in the figure legend acknowledgments!

Now for the animals, thanks of course to all the mice that I used for this project. I like to think my mice were the happiest in the lab, as their main job was to eat. Last but certainly not least, thanks to my very fluffy cats (Meeko, Mouse, and Marbles), who may have played the biggest part in helping me endure these past 6 years.

Works Cited

1. LeDoux, J. The Emotional Brain, Fear, and the Amygdala. *Cell. Mol. Neurobiol.* (2003).
2. Fernandez, A., Molina, D. E. & Hunsperger, R. W. *Central representation of affective reactions in forebrain and brain stem: electrical stimulation of amygdala, stria terminalis, and adjacent structures*. *J. Physiol. (I959)* vol. 45 25–265.
3. Bechara, A. *et al.* Double Dissociation of Conditioning and Declarative Knowledge Relative to the Amygdala and Hippocampus in Humans. **269**, (1995).
4. Johansen, J. P., Cain, C. K., Ostroff, L. E. & LeDoux, J. E. Molecular Mechanisms of Fear Learning and Memory. *Cell* **147**, 509–524 (2011).
5. McCullough, K. M., Morrison, F. G. & Ressler, K. J. Bridging the Gap : Towards a cell-type specific understanding of neural circuits underlying fear behaviors. *Neurobiol. Learn. Mem.* **135**, 27–39 (2016).
6. *Google Trends*. https://trends.google.com/trends/explore?date=all&q=amygdala.
7. Janak, P. H. & Tye, K. M. From circuits to behaviour in the amygdala. *Nature* **517**, 284–292 (2015).
8. Šimić, G. *et al.* Understanding Emotions: Origins and Roles of the Amygdala. *Biomolecules* **11**, 823 (2021).
9. Hagihara, K. M. *et al.* Intercalated amygdala clusters orchestrate a switch in fear state. *Nature* **594**, 403–407 (2021).
10. Ressler, K. J. Amygdala Activity, Fear, and Anxiety: Modulation by Stress. *Biol. Psychiatry* **67**, 1117–1119 (2010).
11. Ledoux, j. E. *Emotion circuits in the brain*. *Annu. Rev. Neurosci* vol. 23 155–184 www.annualreviews.org (2000).

12. Gallagher, M. & Chiba, A. A. The amygdala and emotion. *Curr. Opin. Neurobiol.* **6**, 221–227 (1996).

13. Quirk, G. J., Repa, J. C. & LeDoux, J. E. Fear conditioning enhances short-latency auditory responses of lateral amygdala neurons: Parallel recordings in the freely behaving rat. *Neuron* **15**, 1029–1039 (1995).

14. Campeau, S. & Davis, M. Involvement of the central nucleus and basolateral complex of the amygdala in fear conditioning measured with fear-potentiated startle in rats trained concurrently with auditory and visual conditioned stimuli. *J. Neurosci.* **15**, 2301–2311 (1995).

15. Pribram, K. H., Reitz, S., Mcneil, M. & Spevack, A. A. The effect of amygdalectomy on orienting and classical conditioning in monkeys. **14**, (1979).

16. Gallagher, M., Graham, P. & Holland, P. The amygdala central nucleus and appetitive Pavlovian conditioning: lesions impair one class of conditioned behavior. *J. Neurosci.* **10**, 1906–1911 (1990).

17. Kapp, B. S., Frysinger, R. C., Gallagher, M. & Haselton, J. R. Amygdala central nucleus lesions: Effect on heart rate conditioning in the rabbit. *Physiol. Behav.* **23**, 1109–1117 (1979).

18. Lee, H. J. Role of Amygdalo-Nigral Circuitry in Conditioning of a Visual Stimulus Paired with Food. *J. Neurosci.* **25**, 3881–3888 (2005).

19. Lee, H. J., Gallagher, M. & Holland, P. C. The central amygdala projection to the substantia nigra reflects prediction error information in appetitive conditioning. *Learn. Mem.* **17**, 531–538 (2010).

20. Applegate, C. D., Frysinger, R. C., Kapp, B. S. & Gallagher, M. Multiple unit activity recorded from amygdala central nucleus during Pavlovian heart rate conditioning in rabbit. *Brain Res.* **238**, 457–462 (1982).

21. Cai, H., Haubensak, W., Anthony, T. E. & Anderson, D. J. Central amygdala PKC-δ+ neurons mediate the influence of multiple anorexigenic signals. *Nat. Neurosci.* **17**, 1240–1248 (2014).

22. Ciocchi, S. *et al.* Encoding of conditioned fear in central amygdala inhibitory circuits. *Nature* **468**, 277–282 (2010).

23. Yu, K., Garcia da Silva, P., Albeanu, D. F. & Li, B. Central Amygdala Somatostatin Neurons Gate Passive and Active Defensive Behaviors. *J. Neurosci.* **36**, 6488–6496 (2016).

24. Yu, K. *et al.* The central amygdala controls learning in the lateral amygdala. *Nat. Neurosci.* **20**, 1680–1685 (2017).

25. Fadok, J. P., Markovic, M., Tovote, P. & Lüthi, A. New perspectives on central amygdala function. *Curr. Opin. Neurobiol.* **49**, 141–147 (2018).

26. Kim, J., Zhang, X., Muralidhar, S., LeBlanc, S. A. & Tonegawa, S. Basolateral to Central Amygdala Neural Circuits for Appetitive Behaviors. *Neuron* **93**, 1464-1479.e5 (2017).

27. O'Leary, T. P. *et al.* Neuronal cell types, projections, and spatial organization of the central amygdala. *iScience* **25**, 105497 (2022).

28. Sanford, C. A. *et al.* A Central Amygdala CRF Circuit Facilitates Learning about Weak Threats. *Neuron* **93**, 164–178 (2017).

29. Li, H. *et al.* Experience-dependent modification of a central amygdala fear circuit. *Nat. Neurosci.* **16**, 332–339 (2013).

30. Han, R. T. *et al.* Long-Term Isolation Elicits Depression and Anxiety-Related Behaviors by Reducing Oxytocin-Induced GABAergic Transmission in Central Amygdala. *Front. Mol. Neurosci.* **11**, 246 (2018).

31. van den Burg, E. H. & Stoop, R. Neuropeptide signalling in the central nucleus of the amygdala. *Cell Tissue Res.* **375**, 93–101 (2019).

32. Viviani, D. *et al.* Oxytocin Selectively Gates Fear Responses Through Distinct Outputs from the Central Amygdala. *Science* **333**, 104–107 (2011).

33. Kolber, B. J. *et al.* Central amygdala glucocorticoid receptor action promotes fear-associated CRH activation and conditioning. *Proc. Natl. Acad. Sci.* **105**, 12004–12009 (2008).

34. McCall, J. G. *et al.* CRH Engagement of the Locus Coeruleus Noradrenergic System Mediates Stress-Induced Anxiety. *Neuron* **87**, 605–620 (2015).

35. Andero, R. *et al.* Amygdala-Dependent Molecular Mechanisms of the Tac2 Pathway in Fear Learning. *Neuropsychopharmacology* **41**, 2714–2722 (2016).

36. Anderson, R. I. *et al.* Dynorphin-kappa opioid receptor activity in the central amygdala modulates binge-like alcohol drinking in mice. *Neuropsychopharmacology* **44**, 1084–1092 (2019).

37. Bloodgood, D. W. *et al.* Kappa opioid receptor and dynorphin signaling in the central amygdala regulates alcohol intake. *Mol. Psychiatry* **26**, 2187–2199 (2021).

38. Douglass, A. M. *et al.* Central amygdala circuits modulate food consumption through a positive-valence mechanism. *Nat. Neurosci.* **20**, 1384–1394 (2017).

39. Torruella-Suárez, M. L. *et al.* Manipulations of Central Amygdala Neurotensin Neurons Alter the Consumption of Ethanol and Sweet Fluids in Mice. *J. Neurosci.* **40**, 632–647 (2020).

40. Torruella-Suárez, M. L. & McElligott, Z. A. Neurotensin in reward processes. *Neuropharmacology* **167**, 108005 (2020).

41. Haubensak, W. *et al.* Genetic dissection of an amygdala microcircuit that gates conditioned fear. *Nature* **468**, 270–276 (2010).

42. Sun, Y. & Qian, L. Somatostatin neurons in the central amygdala mediate anxiety by disinhibition of the central sublenticular extended amygdala. (2020) doi:10.1038/s41380-020-00894-1.

43. Botta, P. *et al.* Regulating anxiety with extrasynaptic inhibition. *Nat. Neurosci.* **18**, 1493–1500 (2015).

44. Ahrens, S. *et al.* A Central Extended Amygdala Circuit That Modulates Anxiety. *J. Neurosci.* **38**, 5567–5583 (2018).

45. Wilson, T. D. *et al.* Dual and Opposing Functions of the Central Amygdala in the Modulation of Pain. *Cell Rep.* **29**, 332-346.e5 (2019).

46. Hua, T. *et al.* General anesthetics activate a potent central pain-suppression circuit in the amygdala. *Nat. Neurosci.* **23**, 854–868 (2020).

47. Azuma, S., Yamamoto, T. & Kawamura, Y. Studies on gustatory responses of amygdaloid neurons in rats. *Exp. Brain Res.* **56**, (1984).

48. Sadacca, B. F., Rothwax, J. T. & Katz, D. B. Sodium Concentration Coding Gives Way to Evaluative Coding in Cortex and Amygdala. *J. Neurosci.* **32**, 9999–10011 (2012).

49. Smith, C. M. *et al.* Endogenous central amygdala mu-opioid receptor signaling promotes sodium appetite in mice. *Proc. Natl. Acad. Sci.* **113**, 13893–13898 (2016).

50. Sanchez, M. R. *et al.* Dissecting a disynaptic central amygdala-parasubthalamic nucleus neural circuit that mediates cholecystokinin-induced eating suppression. *Mol. Metab.* **58**, 101443 (2022).

51. Zhang-Molina, C., Schmit, M. B. & Cai, H. Neural Circuit Mechanism Underlying the Feeding Controlled by Insula-Central Amygdala Pathway. *iScience* **23**, 101033 (2020).

52. Ponserre, M., Fermani, F., Gaitanos, L. & Klein, R. Encoding of Environmental Cues in Central Amygdala Neurons during Foraging. *J. Neurosci.* **42**, 3783–3796 (2022).

53. Han, W. *et al.* Integrated Control of Predatory Hunting by the Central Nucleus of the Amygdala. *Cell* **168**, 311-324.e18 (2017).

54. Hardaway, J. A. *et al.* Central Amygdala Prepronociceptin-Expressing Neurons Mediate Palatable Food Consumption and Reward. *Neuron* **102**, 1037-1052.e7 (2019).

55. Ma, H. *et al.* TRPC5 deletion in the central amygdala antagonizes high-fat diet-induced obesity by increasing sympathetic innervation. *Int. J. Obes.* **46**, 1544–1555 (2022).

56. Wang, Y. *et al.* The role of somatosensory innervation of adipose tissues. *Nature* **609**, 569–574 (2022).

57. Sternson, S. M. & Eiselt, A.-K. Three Pillars for the Neural Control of Appetite. *Annu. Rev. Physiol.* **79**, 401–423 (2017).

58. Vohra, M. S., Benchoula, K., Serpell, C. J. & Hwa, W. E. AgRP/NPY and POMC neurons in the arcuate nucleus and their potential role in treatment of obesity. *Eur. J. Pharmacol.* **915**, 174611 (2022).

59. Myers, M. G., Cowley, M. A. & Münzberg, H. Mechanisms of Leptin Action and Leptin Resistance. *Annu. Rev. Physiol.* **70**, 537–556 (2008).

60. Baik, J.-H. Dopaminergic Control of the Feeding Circuit. *Endocrinol. Metab.* **36**, 229–239 (2021).

61. van Zessen, R., van der Plasse, G. & Adan, R. A. H. Contribution of the mesolimbic dopamine system in mediating the effects of leptin and ghrelin on feeding. *Proc. Nutr. Soc.* **71**, 435–445 (2012).

62. Tyree, S. M. & de Lecea, L. Lateral Hypothalamic Control of the Ventral Tegmental Area: Reward Evaluation and the Driving of Motivated Behavior. *Front. Syst. Neurosci.* **11**, 50 (2017).

63. Ran, C., Boettcher, J. C., Kaye, J. A., Gallori, C. E. & Liberles, S. D. A brainstem map for visceral sensations. *Nature* **609**, 320–326 (2022).

64. Boland, M. Human digestion - a processing perspective: Human digestion - a processing perspective. *J. Sci. Food Agric.* **96**, 2275–2283 (2016).

65. Kara Rogers. *The Digestive System*. (Britannica Educational Publishing, 2010).

66. Lafontan, M. Advances in adipose tissue metabolism. *Int. J. Obes.* **32**, S39–S51 (2008).

67. Ghaben, A. L. & Scherer, P. E. Adipogenesis and metabolic health. *Nat. Rev. Mol. Cell Biol.* **20**, 242–258 (2019).

68. Vázquez-Vela, M. E. F., Torres, N. & Tovar, A. R. White Adipose Tissue as Endocrine Organ and Its Role in Obesity. *Arch. Med. Res.* **39**, 715–728 (2008).

69. Wensveen, F. M., Valentić, S., Šestan, M., Turk Wensveen, T. & Polić, B. Interactions between adipose tissue and the immune system in health and malnutrition. *Semin. Immunol.* **27**, 322–333 (2015).

70. Münzberg, H., Floyd, E. & Chang, J. S. Sympathetic Innervation of White Adipose Tissue: to Beige or Not to Beige? *Physiology* **36**, 246–255 (2021).

71. Zhu, Q. *et al.* Neuroendocrine Regulation of Energy Metabolism Involving Different Types of Adipose Tissues. *Int. J. Mol. Sci.* **20**, 2707 (2019).

72. Blüher, M. Obesity: global epidemiology and pathogenesis. *Nat. Rev. Endocrinol.* **15**, 288–298 (2019).

73. Liu, C. *et al.* The Prevalence of Metabolically Healthy and Unhealthy Obesity according to Different Criteria. *Obes. Facts* **12**, 78–90 (2019).

74. Malik, V. S., Willet, W. C. & Hu, F. B. Nearly a decade on — trends, risk factors and policy implications in global obesity. *Nat. Rev. Endocrinol.* **16**, 615–616 (2020).

75. Finucane, M. M. *et al.* National, regional, and global trends in body-mass index since 1980: systematic analysis of health examination surveys and epidemiological studies with 960 country-years and 9·1 million participants. *The Lancet* **377**, 557–567 (2011).

76. Wang, W. *et al.* Metabolically healthy obesity and unhealthy normal weight rural adults in Xinjiang: prevalence and the associated factors. *BMC Public Health* **21**, 1940 (2021).

77. Body-mass index and cause-specific mortality in 900 000 adults: collaborative analyses of 57 prospective studies. **373**, (2009).

78. Berrington de Gonzalez, A. *et al.* Body-Mass Index and Mortality among 1.46 Million White Adults. *N. Engl. J. Med.* **363**, 2211–2219 (2010).

79. Fontaine, K. R., Redden, D. T., Wang, C., Westfall, A. O. & Allison, D. B. Years of Life Lost Due to Obesity.

80. Forouhi, N. G. & Wareham, N. J. Epidemiology of diabetes. *Medicine (Baltimore)* **47**, 22–27 (2019).

81. Knuth, N. D. *et al.* Metabolic adaptation following massive weight loss is related to the degree of energy imbalance and changes in circulating leptin. *Obes. Silver Spring Md* **22**, 2563–2569 (2014).

82. Fothergill, E. *et al.* Persistent metabolic adaptation 6 years after The Biggest Loser competition. *Obes. Silver Spring Md* **24**, 1612–1619 (2016).

83. Wolfe, B. M. *et al.* Resting metabolic rate, total daily energy expenditure, and metabolic adaptation 6-months and 24-months after bariatric surgery. *Obes. Silver Spring Md* **26**, 862–868 (2018).

84. Aaseth, J. O. & Alexander, J. Postoperative Osteoporosis in Subjects with Morbid Obesity Undergoing Bariatric Surgery with Gastric Bypass or Sleeve Gastrectomy. *Nutrients* **15**, 1302 (2023).

85. Navarini, D. *et al.* Predictive Factors of Gastroesophageal Reflux Disease in Bariatric Surgery: a Controlled Trial Comparing Sleeve Gastrectomy with Gastric Bypass. *Obes. Surg.* **30**, 1360–1367 (2020).

86. Rai, A. K., Roy, K., Das, R. & Verma, S. K. Semaglutide: An expedition on last approved glucagon-like peptide-1 analog of past decade. **13**, (2021).

87. Katsurada, K. *et al.* Endogenous GLP-1 acts on paraventricular nucleus to suppress feeding: Projection from nucleus tractus solitarius and activation of corticotropin-releasing hormone, nesfatin-1 and oxytocin neurons. *Biochem. Biophys. Res. Commun.* **451**, 276–281 (2014).

88. Borgmann, D. *et al.* Gut-brain communication by distinct sensory neurons differently controls feeding and glucose metabolism. *Cell Metab.* **33**, 1466-1482.e7 (2021).

89. Jiang, Y. *et al.* GLP-1 Improves Adipocyte Insulin Sensitivity Following Induction of Endoplasmic Reticulum Stress. *Front. Pharmacol.* **9**, 1168 (2018).

90. FAOSTAT. https://www.fao.org/faostat/en/#data/FS.

91. Fernandez, M. L. *et al.* Highlights of Current Dietary Guidelines in Five Continents. *Int. J. Environ. Res. Public. Health* **18**, 2814 (2021).

92. Mobasseri, M. *et al.* Prevalence and incidence of type 1 diabetes in the world: a systematic review and meta-analysis. *Health Promot. Perspect.* **10**, 98–115 (2020).

93. Li, M. *et al.* Gut–brain circuits for fat preference. *Nature* **610**, 722–730 (2022).

94. Rahmouni, K. Leptin-Induced Sympathetic Nerve Activation: Signaling Mechanisms and Cardiovascular Consequences in Obesity. *Curr. Hypertens. Rev.* **6**, 104–209 (2010).

95. Imai, J. & Katagiri, H. Regulation of systemic metabolism by the autonomic nervous system consisting of afferent and efferent innervation. *Int. Immunol.* **34**, 67–79 (2022).

96. Xiao, X. *et al.* A Genetically Defined Compartmentalized Striatal Direct Pathway for Negative Reinforcement. *Cell* **183**, 211-227.e20 (2020).

97. Zhang, X. *et al.* Genetically identified amygdala–striatal circuits for valence-specific behaviors. *Nat. Neurosci.* **24**, 1586–1600 (2021).

98. Furlan, A. *et al.* Neurotensin neurons in the extended amygdala control dietary choice and energy homeostasis. *Nat. Neurosci.* **25**, 1470–1480 (2022).

99. Nguyen, K. P., O'Neal, T. J., Bolonduro, O. A., White, E. & Kravitz, A. V. Feeding Experimentation Device (FED): A flexible open-source device for measuring feeding behavior. *J. Neurosci. Methods* **267**, 108–114 (2016).

100. Deng, H. *et al.* A genetically defined insula-brainstem circuit selectively controls motivational vigor. *Cell* **184**, 6344-6360.e18 (2021).

101. Little, T. Oral and gastrointestinal sensing of dietary fat and appetite regulation in humans: modification by diet and obesity. *Front. Neurosci.* **1**, (2010).

102. Rolls, E. T. Taste, olfactory and food texture reward processing in the brain and obesity. *Int. J. Obes.* **35**, 550–561 (2011).

103. Roelands, C. J. A., Vlugter, J. C. & Waterman, H. I. The Viscosity-Temperature-Pressure Relationship of Lubricating Oils and Its Correlation With Chemical Constitution. *J. Basic Eng.* **85**, 601–607 (1963).

104. Xuewu, Z. *et al.* Rheological models for xanthan gum. *J. Food Eng.* **27**, 203–209 (1996).

105. Marvyn, P. M., Bradley, R. M., Mardian, E. B., Marks, K. A. & Duncan, R. E. Data on oxygen consumption rate, respiratory exchange ratio, and movement in C57BL/6J female mice on the third day of consuming a high-fat diet. *Data Brief* **7**, 472–475 (2016).

106. Patel, J. M. *et al.* Sensory perception drives food avoidance through excitatory basal forebrain circuits. *eLife* **8**, e44548 (2019).

107. Patel, J. M. *et al.* Sensory perception drives food avoidance through excitatory basal forebrain circuits. (2019) doi:10.7554/eLife.44548.001.

108. Kelsch, W., Lin, C.-W., Mosley, C. P. & Lois, C. A Critical Period for Activity-Dependent Synaptic Development during Olfactory Bulb Adult Neurogenesis. *J. Neurosci.* **29**, 11852–11858 (2009).

109. Xue, M., Atallah, B. V. & Scanziani, M. Equalizing excitation–inhibition ratios across visual cortical neurons. *Nature* **511**, 596–600 (2014).

110. Lin, C.-W. *et al.* Genetically Increased Cell-Intrinsic Excitability Enhances Neuronal Integration into Adult Brain Circuits. *Neuron* **65**, 32–39 (2010).

111. Aklan, I. *et al.* NTS Catecholamine Neurons Mediate Hypoglycemic Hunger via Medial Hypothalamic Feeding Pathways. *Cell Metab.* **31**, 313-326.e5 (2020).

112. Tsai, V. W.-W. *et al.* GDF15 mediates adiposity resistance through actions on GFRAL neurons in the hindbrain AP/NTS. *Int. J. Obes.* **43**, 2370–2380 (2019).

113. Chen, J. *et al.* A Vagal-NTS Neural Pathway that Stimulates Feeding. *Curr. Biol.* **30**, 3986-3998.e5 (2020).

114. Izumida, Y. *et al.* Glycogen shortage during fasting triggers liver–brain–adipose neurocircuitry to facilitate fat utilization. *Nat. Commun.* **4**, 2316 (2013).

115. Zhang, X. & Li, B. Population coding of valence in the basolateral amygdala. *bioRxiv* 321232 (2018) doi:10.1101/321232.

116. Pnevmatikakis, E. A. & Giovannucci, A. NoRMCorre: An online algorithm for piecewise rigid motion correction of calcium imaging data. *J. Neurosci. Methods* **291**, 83–94 (2017).

117. Zhou, P. *et al.* Efficient and accurate extraction of in vivo calcium signals from microendoscopic video data. *eLife* **7**, e28728 (2018).

118. Sheintuch, L. *et al.* Tracking the Same Neurons across Multiple Days in Ca2+ Imaging Data. *Cell Rep.* **21**, 1102–1115 (2017).